

The dynamics and high-energy emission of conductive gas clouds in supernova-driven galactic superwinds

A. Marcolini¹, D.K. Strickland², A. D’Ercole³, T.M. Heckman², and C.G. Hoopes²

¹ *Dipartimento di Astronomia, Università di Bologna, via Ranzani 1, 44127 Bologna, Italy.*

² *Department of Physics and Astronomy, Johns Hopkins University, 3400 N. Charles St., Baltimore, MD 21218, USA.*

³ *Osservatorio Astronomico di Bologna, via Ranzani 1, 44127 Bologna, Italy.*

Accepted ..., Received ...; in original form...

ABSTRACT

Superwinds from starburst galaxies are multi-phase outflows that sweep up and incorporate ambient galactic disk and halo gas. The interaction of this denser material with the more diffuse hot wind gas is thought to give rise to the OVI emission and absorption in the far Ultraviolet (FUV) and the soft thermal X-ray emission observed in superwinds. In this paper we present high-resolution hydrodynamical models of warm ionized clouds embedded in a superwind, and compare the OVI and soft X-ray properties to the existing observational data. These models include thermal conduction, which we show plays an important role in shaping both the dynamics and radiative properties of the resulting wind/cloud interaction. Heat conduction stabilizes the cloud by inhibiting the growth of Kelvin-Helmholtz and Rayleigh-Taylor instabilities, and also generates a shock wave at the cloud’s surface that compresses the cloud. This dynamical behaviour influences the observable properties. We find that while OVI emission and absorption always arises in cloud material at the periphery of the cloud, most of the soft X-ray arises in the region between the wind bow shock and the cloud surface, and probes either wind or cloud material depending on the strength of conduction and the relative abundances of the wind with respect to the cloud. In general only a small fraction ($\lesssim 1\%$) of the wind mechanical energy intersecting a cloud is radiated away at UV and X-ray wavelengths, with more wind energy going into accelerating the cloud. Clouds in relatively slow cool winds radiate a larger fraction of their energy, which are inconsistent with observational constraints. Models with heat conduction at Spitzer-levels are found to produce observational properties closer to those observed in superwinds than models with no thermal conduction, in particular in terms of the OVI-to-X-ray luminosity ratio, but cloud life times are uncomfortably short ($\lesssim 1$ Myr) compared to the dynamical ages of real winds. We experimented with reducing the thermal conductivity for one set of model parameters, and found that even when we reduced conduction by a factor of 25 that the simulations retained the beneficial hydrodynamical stability and low OVI-to-X-ray luminosity ratio found in the Spitzer-level conductive models, while also having reduced evaporation rates. Although more work is required to simulate clouds for longer times and to investigate cloud acceleration and thermal conduction at sub-Spitzer levels in a wider range of models, we conclude that thermal conduction can no longer be ignored in superwinds.

Key words: ISM: clouds – ISM: jets and outflows – galaxies: starburst – ultraviolet: galaxies – X-rays: galaxies

1 INTRODUCTION

Superwinds are multi-phase, loosely-collimated galaxy-sized outflows with measured velocities in excess of several hundred to a thousand kilometers per second, driven from galaxies experiencing intense recent or ongoing star-formation,

i.e. starburst galaxies. These superwinds are common in the local Universe, occurring in nearly all galaxies classified as undergoing starburst activity (Lehnert & Heckman 1995; Heckman 1998), and appear ubiquitous among the Lyman break galaxies at redshift ~ 3 where they are blowing

~ 100 kpc sized holes in the inter-galactic medium (e.g. Pettini et al. 2001; Adelberger et al. 2003).

Superwinds are believed to be driven by the thermal and ram pressure of an initially very hot ($T \sim 10^8$ K), high pressure ($P/k \sim 10^7 \text{ K cm}^{-3}$) and low density wind, itself created from the merged remnants of very large numbers of core-collapse supernovae (SNe), and to a lesser extent the stellar winds from the massive stars, that occur over the ~ 100 Myr duration of a typical starburst event (Chevalier & Clegg 1985). The thermalized SN and stellar wind ejecta predicted by this model (which we shall call the wind fluid for convenience) is too hot and too tenuous to be easily observed (unless heavily mass-loaded, e.g. Suchkov et al. 1996), but hydrodynamical models of superwinds show that the wind fluid sweeps up and incorporates larger masses of ambient galactic disk and halo interstellar medium (ISM) into the superwind, material which is more easily detected observationally (Chevalier & Clegg 1985; Suchkov et al. 1994; Strickland & Stevens 2000).

Indeed, the majority of nearby superwinds have been discovered using optical imaging and spectroscopy to identify outflow in the warm ionized gas (gas at $T \sim 10^4$ K), in many cases directly imaging bipolar structures aligned with the host galaxy minor axis with kinematics indicative of outflow at velocities of $v_{\text{WIM}} = \text{a few } \times 100 \text{ to } 1000 \text{ km s}^{-1}$ (e.g. Axon & Taylor 1978; McCarthy, Heckman, & van Breugel 1987; Heckman, Armus, & Miley 1987, 1990; Bland & Tully 1988; Heckman, Armus, & Miley 1990; Lehnert & Heckman 1995, 1996). Superwinds from galaxies at high redshift are recognized by virtue of blue-shifted interstellar absorption lines from warm-neutral and warm-ionized gas species (e.g. Pettini et al. 2000; Frye et al. 2002; Adelberger et al. 2003), absorption features very similar to those seen in local starburst galaxies with superwinds (Phillips 1993; Kunth et al. 1998; González Delgado et al. 1998; Heckman et al. 2000). Nearby superwinds have also been extensively studied in soft X-ray emission (e.g. Read et al. 1997; Dahlem et al. 1998; Strickland et al. 2004) which probes emission from hot gas with temperatures in the range $T \sim 10^6$ to 10^7 K, following their initial detection by *Einstein* X-ray observatory (Watson, Stanger, & Griffiths 1984; Fabbiano & Trinchieri 1984). Indeed, observations have demonstrated that all phases of the ISM found in normal late type galaxies are also incorporated into starburst-driven superwinds (e.g., see the reviews of Bland-Hawthorn 1995; Dahlem 1997).

Over the last 5 years new observations of superwinds, in particular spaced-based observations of OVI absorption and emission from $T \sim 10^{5.5}$ K gas in the FUV, and thermal emission from $T \sim 10^{6-7}$ K gas in X-ray regime, have substantially added to our understanding of the multi-wavelength properties of superwinds (Strickland et al. 2000; Heckman et al. 2001b, 2002; Strickland et al. 2002; Otte et al. 2003; Aloisi et al. 2003; Hoopes et al. 2003). These observations have shown that the majority of the soft X-ray emission in superwind is not due a volume-filling wind fluid, but that it and the OVI-emitting and absorbing gas arise in some form of interaction between the wind fluid and denser ambient disk or halo ISM. This is in qualitative agreement with some of the analytical and theoretical models mentioned above. The observations, in particular those of OVI, are not easily explained by the simple analytical models of wind-blown bubbles (Weaver et al. 1977;

Mac Low & McCray 1988) often applied to superwinds (see e.g. Heckman et al. 2001b).

Chevalier & Clegg (1985) first posited that both the optical nebular emission and the soft X-ray emission in superwinds (as had been observed by Axon & Taylor 1978; Watson et al. 1984, for example) is from shocks driven into clouds embedded in a high velocity wind of merged SN ejecta, primarily as the observed soft X-ray luminosities exceeded the predicted emission for the wind fluid. Later optical and low-spatial resolution X-ray observations were interpreted in the light of interactions between the wind fluid and ambient ISM, either with entrained cloud or with ambient disk or halo ISM at the walls of the outflow cavity (McCarthy et al. 1987; Heckman et al. 1990; Suchkov et al. 1994). In this picture clouds are either dense pre-existing structure over-run and incorporated into the wind, or generated at the cavity walls through the action of instabilities in the shell of swept-up ambient ISM (primarily either shell fragmentation through Rayleigh Taylor instabilities when the superbubble blows out of the disk, or dense gas ripped off the walls of the outflow cavity by Kelvin-Helmholtz instabilities). High resolution optical observations of superwinds show small scale clumps in the H α filaments of NGC 3079 and M82 with sizes of $\sim 20 - 30$ pc, often associated with fainter elongated structures (Cecil et al. 2001; Ohyama et al. 2002). These are similar to the tadpole-like clouds found in simulations (Suchkov et al. 1994; Strickland & Stevens 2000). The basic wind/ISM interaction model for soft X-ray emission in superwinds is validated by modern high resolution X-ray observations (Strickland et al. 2000, 2002; Strickland 2002; Cecil et al. 2002; Schurch et al. 2002; Strickland et al. 2004), which show the soft X-ray emission is structured very similarly to optical H α emission on scales from kpc down to as small as $10 - 20$ pc, with filaments, clumps and apparently limb-brightened walls. Much of this H α and soft X-ray structure is associated with large-scale filaments or the edges of the superwind, but examples of wind interactions with clouds or larger-scale obstacles exist, e.g. most-notably the M82 northern cloud (Devine & Bally 1999; Lehnert et al. 1999).

Returning to the issue of OVI absorption and emission in superwinds, a wind/cloud interaction model is considered most plausible for explaining the absorption properties of neutral, warm photoionized and coronal phase gas in NGC 1705 (Heckman et al. 2001b). The kinematics and column density of the OVI-absorbing gas are inconsistent with the standard superbubble model, where the coronal phase gas arises in a conduction front at the walls of the superbubble shell (Castor et al. 1975; Weaver et al. 1977). In NGC 1705, the superbubble shell (traced by warm photoionized gas) has almost certainly ruptured, and is expanding more slowly than the OVI-absorbing gas. The most likely explanation of the data is that the OVI-absorbing gas is being generated as the hot gas from the interior of the bubble flows out past fragments of the ruptured superbubble shell.

In this paper we present high-resolution hydrodynamical models of warm ionized clouds embedded in a superwind, and compare the simulated OVI and soft X-ray properties to the existing observational data. The interaction of a superwind with an embedded cool cloud is not the only form of wind/ISM interaction considered important in superwinds, but wind/cloud interactions undoubtedly do occur within

superwinds and we shall focus on them in this paper. These models include the effect of thermal conduction, which we show plays an important role in shaping both the dynamics and radiative properties of the resulting wind/cloud interaction. Thermal conduction has long been suspected as being an important process in superwinds, but has not been included in hydrodynamical models of superwinds (with the exception of one model by D’Ercole & Brighenti 1999). Simulations of cool clouds embedded in a hot fluid, including the effects of thermal conduction, have been performed before (Ferrara & Shchekinov 1993; Vieser & Hensler 2000). However, the models we present here are the first high-resolution simulations of an ISM cloud embedded in a hot, supersonic, high ram-pressure wind.

The observational diagnostics available from any single waveband study of superwinds¹ are too crude to strongly constrain among the many possible hypotheses available. However, multi-wavelength comparisons, e.g. the spatial location of H α emission compared to the soft X-ray emission, have proved more useful and more robust (e.g. McCarthy et al. 1987; Heckman et al. 1990; Strickland et al. 2000, 2002). The coronal phase gas responsible for OVI emission and absorption in superwinds must either originate from the cooling of originally hotter gas, or is collisionally or conductively heated. In any case, OVI is also a tracer of energetic collisional processes in superwinds in the same way X-ray emission is (Heckman et al. 2002). This is unlike the optical nebula emission in superwinds (e.g. H α and [N II] emission), which can be photo-excited by massive stars or from X-ray irradiation, in addition to collisionally excited in shocks. The effect of extinction by interstellar material at the wavelengths of the OVI doublet is equivalent to the extinction experienced by soft X-rays of energy ~ 0.3 keV, somewhat mitigating the observational uncertainties in the absolute level of extinction. Oxygen is also the main coolant for plasma with temperature between 10^5 and 10^6 K, and second only in importance to Iron as a coolant in hotter gasses. The OVI-absorbing or emitting gas is also the highest temperature phase in superwinds for which the velocity can currently be measured, yielding important clues to the relative kinematics of different phases in superwinds (see e.g. Heckman et al. 2001b). Thus a comparison between the OVI and soft X-ray properties of superwinds should hopefully prove as, if not more, instructive than the H α /X-ray comparisons that have already been made. We have thus chosen to consider simultaneously OVI and the soft X-ray obser-

vational properties of our modeled wind/cloud interactions, in order to better constrain which models, if any, provide a good match to the observed properties of superwinds.

In Section 2 we describe the numerical code employed to perform the models, the parameters of our chosen superwind and cloud model and how we calculate the OVI and X-ray properties thereof. The results of the simulations performed are described in Section 3. The implications of these results for understanding superwinds are discussed in Section 4, followed by a summary of the results in Section 5.

2 THE NUMERICAL METHOD

As a first step in investigating wind/ISM interactions in superwinds, we explore the properties of simple model in which a single dense cloud (initially at rest) is embedded into a supersonic wind of hot gas.

2.1 Simulations

To run the simulations we use the 2D BOH (Bologna Hydrodynamics) hydro-code implemented with the thermal conduction. The code is based on a second-order upwind scheme (Bedogni & D’Ercole 1986), in which consistent advection (Norman, Wilson, & Barton 1980) is implemented to reduce numerical diffusion. We solve the usual hydrodynamic continuity equations. We also include a further tracer variable representative of the cloud material which is passively advected; such a tracer allows us to compute the degree of mixing between the cloud and superwind material.

To take into account the thermal conduction we adopt the operator splitting method. We isolate the heat diffusion term in the energy equation and solve the heat transport equation, alternatively along the z and R direction separately, through the Crank-Nicholson method which is unconditionally stable and second order accurate. The resulting system of implicit finite difference equations is solved according to the two-stage recursion procedure (e.g. Ritchmyer & Morton 1967). Following Cowie & McKee (1977), we adopt saturated fluxes to avoid unphysical heat transport in presence of steep temperature gradients (see below).

In all simulations we adopt 2D cylindrical coordinates. The central area of the computational domain is covered by a uniform grid with mesh size $\Delta R = \Delta z = 0.1$ pc. Beyond some distance to the center the linear mesh size increases geometrically in both directions with a size ratio of 1.07 between adjacent zones. The grid edges are thus at large distances in order to avoid that possible spurious perturbations originating at the boundaries may affect the solution in the central region of interest.

For the RE models (see Section 2.2) the total number of mesh points is 800×400 ($z \times R$), while the uniform grid region is covered by of 600×300 points. For the models with ram pressure the whole grid has 1200×400 ($z \times R$) mesh points i.e. an extension of ~ 3 kpc in length by ~ 1.3 kpc in radius, while the uniform region has 1000×300 points.

In all the models reflecting boundary conditions are enforced on the z -axis. In the RE models, outflow conditions are applied at all the remaining boundaries. For the models with wind velocity $v_w \neq 0$, the superwind flows parallel to

¹ For example, the diagnostic parameters that can be most robustly extracted from observation data are: Soft X-ray emission — X-ray flux and surface brightness, emission-weighted mean temperature, and the apparent gas-phase abundance of O (and some of the other alpha-elements) with respect to Fe. Kinematics and absolute element abundances, and associated parameters such as the emission integral can not currently be obtained or are too uncertain to make use of; OVI emission — fluxes, line-widths and simple kinematics; Optical emission — fluxes and surface-brightnesses, spatially mapped kinematics and standard nebular diagnostics within the inner brighter regions of winds. The nebular emission appears dominated by stellar photo-ionization in the inner region of winds, but in many cases line ratios (in particular H α /[N II]) become more “shock-like” at larger distances from the central starburst.

Table 1. Model parameters for the primary set of superwind/cloud interaction simulations.

Model	ρ_w (g cm ⁻³)	T_w (K)	v_w (km s ⁻¹)	χ	\mathcal{M}	T_{BS} (K)	σ_0	τ_{cc} (10 ⁵ yr)
T1LP(NC)	1×10^{-26}	1×10^6	447	100	2.98	2.8×10^6	0.13	3.3
T1HP(NC)	1×10^{-26}	1×10^6	1000	100	6.66	1.4×10^7	3.27	1.5
T5LP(NC)	2×10^{-27}	5×10^6	1000	500	2.98	1.4×10^7	16.34	3.3
T5HP(NC)	2×10^{-27}	5×10^6	2236	500	6.66	6.9×10^7	396.98	1.5

Model parameters are the same in models with and without (NC) heat conduction. See Section 2.2 for details. Parameters with subscript w refer to the undisturbed wind fluid. The density contrast between the cloud and the undisturbed wind is $\chi = \rho_c/\rho_w$. The wind is super-or-hypersonic with respect to the cloud, with Mach number $\mathcal{M} = v_w/c_{s,w}$. The ratio of wind ram pressure to initial cloud or wind thermal pressure is ~ 15 in the low pressure (LP) models, and ~ 75 in the high pressure (HP) models. The highest temperature in the wind bow shock around each cloud will be approximately the post-shock temperature for a strong shock, i.e. $T_{BS} \approx 3/16 \mu m_H v_w^2/k$. The dimensionless heat flux saturation parameter σ_0 (equation 2) corresponding to this bow shock temperature (assuming the bow shock density $\rho_{BS} = 4\rho_w$) is a relative measure of the *initial* strength of the dynamical effects seen in the conductive models. The time scale for the cloud to be crushed by the shock driven into it is τ_{cc} (equation 4).

the z -axis and enters the grid from right-side of the grid where inflow boundary conditions are applied.

The simulations are run until the cloud, which is accelerated by its interaction with the wind, leaves the computational grid after ~ 1 to 1.5 Myr.

Radiative energy losses within the simulation are taken into account considering the cooling curve Λ for Solar metallicities as parameterized by Mathews & Bregman (1978). Models of stationary conductive clouds run assuming primordial abundances give essentially the same dynamical results. With less cooling, there is slightly more hot gas present ($\sim 10\%$ more by mass), but essentially the soft X-ray and OVI luminosity, and OVI column densities are lower in proportion to the reduction in metallicity. Clearly in these simulations with strong conduction (i.e. at Spitzer levels) the structure of conductive front is not controlled or significantly influenced by radiative cooling, as in that case we would have expected a very significant increase in the total mass of hot gas in the low abundance simulations.

OVI emission originates in a thin layer of the conductive front where the gas is at temperature $T \sim 3 \times 10^5$ K. It is crucial to have a numerical resolution good enough to capture this thin layer in the conductive front. With a cell size of 0.1 pc the OVI emission from our simulations originates from a layer 6-7 grid cells wide. If we reduce the grid resolution by a factor of two (to 0.2 pc) cooling rates are higher, although the increase in L_{OVI} and L_X is a factor of $\lesssim 20\%$ compared to 0.1 pc resolution simulations. This suggests that even at 0.2 pc resolution the conductive front is still marginally resolved at the OVI layer, so that we are confident that the default 0.1 pc resolution simulations are numerical resolving the conductive interface.

2.2 The wind/cloud model

We make the following simplifying assumptions:

- (i) The clouds are initially spherical.
- (ii) The clouds are initially in pressure equilibrium with the ambient gas.
- (iii) The cloud self-gravity is neglected.

(iv) Magnetic fields are neglected.

(v) The gas is not allowed to cool below $T = 10^4$ K.

(vi) Non-equilibrium ionization effects on the cooling curve are neglected.

(vii) The elemental abundances of both the wind and cloud material are Solar.

Assumptions (i) and (ii) are made to make simpler initial conditions. However, they do not influence very much the results because, as it will be described in Section 3, dynamical effects will quickly destroy both the spherical shape and the pressure equilibrium of the cloud. About assumption (iii), it is easy matter to show that, for the cloud parameters adopted in this paper (see below) the cloud mass results always lower than the cloud Jeans mass, even computed taking into account external pressure (see e.g. Shu 1992). In spite assumption (iv), we actually consider in Section 3.7 the possibility of a reduced value of the thermal conductivity due to the presence of magnetic fields. Point (v) assumes that the ionizing radiation field due to the massive stars in the stellar burst is able to hold the cloud ionized. Assumptions (vi) and (vii) are discussed in Section 2.3 and Section 4.3, respectively.

The cloud properties, and the range in wind properties, we consider are consistent with observational and numerical studies of superwinds. At the location of the *FUSE* aperture used to survey OVI emission in M82 and NGC 3079 (Hoopes et al. 2003, Hoopes et al, in preparation), the H α -observations of Ohya et al. (2002) and Cecil et al. (2001) show $\sim 20 - 30$ pc-scale clumps within the kpc-long filaments. The cloud-like structures visible in the highest resolution hydrodynamical simulations of Strickland & Stevens (2000) have diameters of ~ 30 pc, mass density $\sim 10^{-24}$ g cm⁻³, and are embedded in wind fluid with a range of wind velocity, density and ram pressure similar to those we assume.

We run different models of an evaporating cloud embedded into a galactic wind. In most of the models the cloud properties are the same: radius $R_c = 15$ pc, temperature $T_c = 10^4$ K and cloud mass density $\rho_c = 10^{-24}$ g cm⁻³ (proton number density $n_c = 0.42$ cm⁻³). The cloud mass

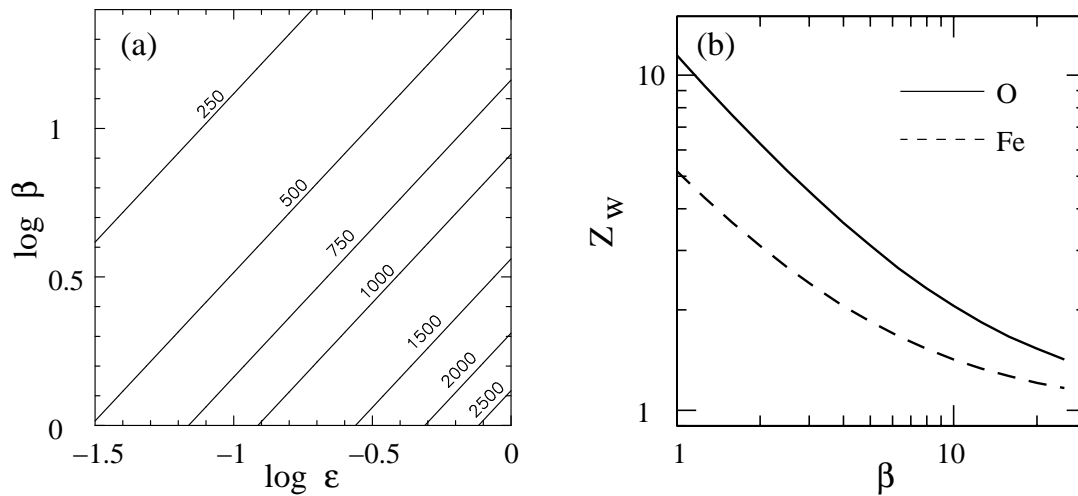


Figure 1. (a) Superwind terminal velocity (in km/s) as a function of the efficiency of supernova energy thermalization ϵ and the factor by which the hot wind fluid is mass-loaded β . (b) Oxygen and Iron abundance in units of standard Solar abundance as a function of β , assuming the ambient medium has Solar abundances. See Section 2.2 for details.

is $\sim 210M_\odot$. We consider two sets of values for the density n_w and the temperature T_w of the superwind, both having the same thermal pressure $P = 1.3 \times 10^{-12}$ dyne cm^{-2} : $(\rho_w, T_w) = (10^{-26} \text{ g cm}^{-3}, 10^6 \text{ K})$, $(\rho_w, T_w) = (2 \times 10^{-27} \text{ g cm}^{-3}, 5 \times 10^6 \text{ K})$. The cloud is thus initially in thermal pressure equilibrium with the wind in all the models. We further considered two possible values of the ram pressure exerted by the superwind on the cloud, namely $P_{\text{ram}} = 2 \times 10^{-11}$ dyne cm^{-2} (low ram pressure models, model name suffix LP), and $P_{\text{ram}} = 10^{-10}$ dyne cm^{-2} (high ram pressure models, model name suffix HP).

Each model is specified by the values of superwind temperature and ram pressure: for instance, the model T5LP is characterized by $(n_w, T_w) = (8.3 \times 10^{-4} \text{ cm}^{-3}, 5 \times 10^6 \text{ K})$ and $P_{\text{ram}} = 2 \times 10^{-11}$ dyne cm^{-2} or, equivalently, a superwind velocity with respect to the cloud of $v_w = 1000 \text{ km s}^{-1}$ (see Table 1). To elucidate the role of the cloud size we also ran a model equivalent to model T1LP, but with a cloud radius $R_c = 45 \text{ pc}$ and with a factor 3 lower resolution.

For convenience we have chosen to treat the density, velocity and metal abundance of the wind fluid as separate variables whose values are not correlated. However, theoretically these variables are not independent of each other, as mass loaded winds will have lower velocity and lower metallicity (see e.g. Suchkov et al. 1996). To place the wind model parameters shown in Table 1 in context we show the wind terminal velocity and Oxygen and Iron abundances as a function of SN energy thermalization efficiency ϵ and mass-loading β in Fig. 1. The values shown were calculated using the energy and mass return rates and elemental yields from SNe and stellar winds from version 4 of Starburst99 (Leitherer et al. 1999). We assumed continuous star-formation of $1M_\odot/\text{yr}$ at a time 30 Myr after the first star formation from gas of Solar abundances, but the variation in v_w or Z_w from assuming a different star formation history, time or initial metallicity is typically $\lesssim 30\%$. The mass injection rate in the starburst $\dot{M} = \beta \times \dot{M}_{\text{SN}}$, where \dot{M}_{SN} is the mass injection rate due to SNe and stel-

lar winds alone and β is the degree of mass-loading. The terminal velocity in the hot wind fluid in Chevalier & Clegg (1985) superwind model is $v_\infty = (2\dot{E}/\dot{M})^{0.5} \approx 2800(\epsilon/\beta)^{0.5}$. To first order the density of the wind fluid scales as $\beta^{1.5}$. If the elemental abundance of any particular element i is $Z_{i,\text{SN}}$ in the SN and stellar wind ejecta, and $Z_{i,\text{ISM}}$ in the ambient ISM, then metal abundance in the wind fluid will be $Z_{i,W} = \beta^{-1} \times (Z_{i,\text{SN}} + [\beta - 1] \times Z_{i,\text{ISM}})$. On the Anders & Grevesse (1989) abundance scale $Z_{O,\text{SN}} \sim 11.5Z_{O,\odot}$ and $Z_{\text{Fe},\text{SN}} \sim 5.2Z_{\text{Fe},\odot}$.

In order to disentangle the effect of the heat conduction from that due to the ram pressure, we also ran models without heat conduction (model suffix NC) as well as models of evaporating clouds in a static hot medium (model prefix RE). The model analogous to T5LP, but without heat conduction, is called T5LPNC. This primary set of eight models are summarized in Table 1. We also ran two models equivalent to the model with conduction T5LP, but with values of the coefficient of thermal conductivity that have been reduced by factors 5 and 25 below the Spitzer value. A further model equivalent to model T1LP except with a cloud radius of $R_c = 45 \text{ pc}$ was performed to investigate how the wind/cloud interaction depends on cloud size. The static medium models are characterized only by the superwind temperature, thus, for instance, the model analogous to T5LP is called RE05 (see Table 2).

2.3 Analysis

Calculations of the luminosity, 2-dimensional volume emissivities, and OVI column densities from these models we performed separately from the simulations themselves. As stated above, we assume that the plasma is in collisional ionization equilibrium. The electron and ion temperatures in each computational cell are thus $T = (\mu m_{\text{H}} P)/(k\rho)$, where k is the Boltzmann constant, P the thermal pressure, ρ the total mass density, and μm_{H} is the mean mass per particle.

Table 2. Model parameters for models of a cold cloud in a stationary hot medium.

Model	ρ_w (g cm ⁻³)	T_w (K)	χ	σ_0
RE01	1×10^{-26}	1×10^6	100	0.07
RE05	2×10^{-27}	5×10^6	500	8.59
RE10	1×10^{-27}	1×10^7	1000	68.70

Parameters with subscript w refer to the static hot medium surrounding the cloud. The density contrast between the cloud and the hot medium is $\chi = \rho_c/\rho_w$. The dimensionless heat flux saturation parameter σ_0 is described in Section 3.1, equation 2.

For the highly-ionized coronal and hot gas phases we are interested in we use a value of $\mu m_H = 1.02 \times 10^{-24}$ g cm⁻³.

In the low density limit the power emitted in some energy band E , in units of ergs⁻¹, from a elemental volume δV is $\delta L_E = n_e n_H \Lambda_E(T, Z) \delta V$, where $\Lambda_E(T, Z)$ is the emissivity at temperature T , for metal-abundance Z in energy band E . For a given mass density ρ and Solar abundances, then to good accuracy $n_H = \mathcal{X}_H \rho/m_H$ and $n_e = 0.5(1 + \mathcal{X}_H)\rho/m_H$, where \mathcal{X}_H is the Hydrogen mass fraction. We use a value of $\mathcal{X}_H = 0.7057$. Making use of the assumed symmetry around the z -axis, we sum the luminosity over all cells within a cylindrical volume chosen to encompass the cloud and the majority of the wind bow-shock and any cloud fragments. We ignore any absorption of this emission from material on the computational grid.

For the purposes of displaying which regions are the strongest OVI and soft X-ray emitters we plot 2-dimensional maps of volume emissivity, i.e. emission per unit volume $\delta L_E/\delta V = n_e n_H \Lambda_E(T, Z)$, in units of erg s⁻¹ cm⁻³.

The OVI emissivities we use are based on the MEKAL hot plasma code (Mewe et al. 1985; Kaastra & Mewe 1993; Mewe et al. 1995; Liedahl et al. 1995). Note that the luminosity quoted is the sum of the two lines in the $\lambda = 1032$ Å and 1038 Å doublet.

The soft X-ray luminosities we quote are in the $E = 0.3 - 2.0$ keV energy band, chosen to correspond to the energy band used in the *Chandra* ACIS observations we compare to. The X-ray emissivities used are based on the 1993 update to the Raymond & Smith (1977) hot plasma code. Although the Raymond & Smith code is no longer suitable for detailed X-ray spectroscopy, the broad-band emissivities it predicts are reasonably accurate. In the chosen energy band the difference between the broad-band soft X-ray emissivities given by the Raymond & Smith code and the MEKAL code are $\sim 20\%$ for gas with $10^6 < T < 10^7$ K, and within a few percent for hotter gas.

Given that the physical size of the observational *FUSE* 30'' aperture depends on the distance to the observed galaxies (equivalent to ~ 530 pc for M82, and for ~ 1.4 kpc for NGC 891, the closest and more distant galaxies we compare to), and that we do not know how many clouds actually lie within these regions, our quantitative comparison to the observational data will concentrate on the ratio of OVI to soft X-ray emission, rather than the absolute emitted luminosities. The physical volume represented by the full computational grid is much larger than the volume we would realistically expect to be occupied by only a single cloud in a superwind, and the X-ray emission from this volume is

dominated by the wind, rather than wind/cloud interaction. We therefore calculate the emission within a smaller cylindrical region judged large enough to encompass the cloud and the most luminous part of the bow shock. This region extends 20 pc upstream and 80 pc downstream of the initial center of the cloud, and out to a radius of 50 pc.

We also calculate the predicted OVI column densities through the models, using an updated version of the code first used in Heckman et al. (2001b). Along any incremental path length Δl , the incremental OVI column density $\Delta N_{\text{OVI}} = \Delta l n_H f_{\text{OVI}}(T) A_{\text{O}}$, where n_H is the local hydrogen number density and A_{O} is the fractional abundance of oxygen atoms with respect to hydrogen ($A_{\text{O}} = 8.51 \times 10^{-4}$ for Solar abundance in the Anders & Grevesse 1989 scale). In collisional ionization equilibrium, and at the low densities found in our simulations, the fraction of oxygen atoms in the OVI state is purely a function of temperature $f_{\text{OVI}}(T)$, the values for which we take from Sutherland & Dopita (1993).

The column density is evaluated along between 10 and 120 lines of sight through each simulation volume. For convenience we calculate lines of sight parallel to the z -axis (i.e. parallel to the wind) and within a radius R , which may be larger or smaller than the actual radius of the cloud. The net OVI column density quoted is the appropriately-weighted average OVI column density over all lines of sight. Column densities calculated using larger radii are typically lower than the peak N_{OVI} column density that can be found using a single line of sight, or even the average over a radius $R \lesssim R_c$. Obviously the average OVI column density will be reduced if many lines of sight do not intersect any gas in the temperature range in which the OVI ion is abundant. Within the region of space probed by a typical *FUSE* LWRs aperture there are probably many clouds, but as their areal covering factor may in some cases be less than unity is worthwhile calculating N_{OVI} over radii $R \gtrsim R_c$.

Cooling rates in all the hydrodynamical calculations assume Solar abundances (as given in Anders & Grevesse 1989, which is the commonly used standard in X-ray astronomy). Although we track the contribution of cloud and wind material to the gas density in each computational cell and hence calculate the mean metal abundance within each cell, for the purpose of calculating the radiative cooling we assume $Z_w = Z_c = 1.0 \times Z_{\odot}$. In reality cloud and wind material are likely to have different metal abundances, with the metal abundance of the wind depending on the degree of mass-loading. We shall demonstrate later that the rate of cooling within the wind is not dynamically significant. This allows us to post-facto consider the relative contribution of wind and cloud material to the X-ray and OVI emission in cases when $Z_w \neq Z_c$. We shall discuss this issue further in Section 4.

For each computational cell i, j we assess the relative contribution by mass from wind material $\mathcal{R}_{ij} = \rho_{w,ij}/(\rho_{w,ij} + \rho_{c,ij})$. We assume that the wind and cloud material in each cell mix to form a mixture with metallicity $Z_{ij} = (Z_w \rho_{w,ij} + Z_c \rho_{c,ij})/(\rho_{w,ij} + \rho_{c,ij}) = Z_c + \mathcal{R}_{ij}(Z_w - Z_c)$. Which material dominates the emission from the system is then the luminosity-weighted sum of \mathcal{R}_{ij} ,

$$\langle \mathcal{R} \rangle = \frac{\sum L_{ij} \mathcal{R}_{ij}}{\sum L_{ij}},$$

taking into account the metallicity dependence of the lumi-

osity due to each cell L_{ij} . The mean metal abundance that would be observed $\langle Z \rangle$, for example in the X-ray band, would be the luminosity-weighted sum of Z_{ij} . Mathematically this is equivalent to $\langle Z \rangle = Z_c + \langle \mathcal{R} \rangle (Z_w - Z_c)$.

Calculations following the exact ionization balance of the wind and cloud material are currently beyond our capability. We shall show that radiative cooling is not dynamically important, but given our interest in the FUV and X-ray absorption and emission predicted by these models we shall briefly discuss the issue of non-equilibrium effects. Non-ionization equilibrium cooling calculations show that the emissivity differs most from the equilibrium case for gas with a temperature $T < 10^6$ K. Nevertheless, OVI column densities and Oxygen resonance line emissivities differ from the equilibrium values by factors of at most $\sim 2 - 3$ (Edgar & Chevalier 1986; Sutherland & Dopita 1993). The latter paper demonstrates that the OVI ion is most abundant in non-equilibrium cooling conditions at the same kinetic temperature as in collision equilibrium. Considering initially low-ionization gas being conductively evaporated, the OVI column density may be increased by a factor of ~ 3 from the equilibrium case (Weaver et al. 1977; Indebetouw & Shull 2004), as the region of OVI ions extends into lower density and kinetically hotter material (the gas is under-ionized, in contrast to the over-ionized state in a cooling plasma). Weaver et al. show that this leads to a minor reduction in soft X-ray luminosity, but it is not clear in which direction and by how much the OVI luminosity changes. Thus we believe the cooling rates and column densities we calculate assuming collisional equilibrium are most likely accurate to within a factor ~ 3 . This magnitude of effect is not large enough to alter our conclusions in a significant manner.

3 RESULTS

The main purpose of the present paper is the study of the OVI and X-ray properties of conductively-evaporative cold clouds embedded in a hot superwind. However, before to present the results obtained for this scenario, it is instructive to consider the behaviour of the cloud in two extreme cases: *i*), one in which the evaporating cloud is at rest relative to the hot gas, and *ii*), one in which the cloud swept by the superwind does not suffer any evaporative mass loss (i.e. thermal conduction is completely suppressed).

3.1 Evaporating clouds at rest in a static hot medium (RE models)

The first approach to the problem of the effects of thermal conduction on a cool cloud embedded in a hot medium has been undertaken by Cowie & McKee (1977). In the classical diffusion approximation of thermal conduction they obtained an analytical solution for the mass loss rate of an evaporating cloud given by

$$\dot{M}_{\text{cl}} = 4.34 \times 10^{-7} T_6^{5/2} R_{\text{c,pc}} \text{ M}_{\odot} \text{ yr}^{-1}, \quad (1)$$

where $T_6 = T/(10^6 \text{ K})$ is the temperature of the ambient gas, and $R_{\text{c,pc}} = R_{\text{c}}/(1 \text{ pc})$ is the cloud radius. In addition, they pointed out that the classical diffusion approximation breaks down when the mean free path of electrons becomes larger than the temperature scale (saturation). The relevance of

this effect is quantified by the dimensionless parameter σ_0 defined as

$$\sigma_0 = 4.22 \times 10^{-3} \frac{T_6^2}{n_{\text{H}} R_{\text{c,pc}}}, \quad (2)$$

where n_{H} is the number density of hydrogen atoms in the ambient gas (not the number density within the cloud). In the saturated regime ($\sigma_0 > 1$) the evaporation rate is given by Cowie et al. (1981):

$$\dot{M} = 1.36 \dot{M}_{\text{cl}} \sigma_0^{-5/8}. \quad (3)$$

The above results are obtained in the assumption of steady, isobaric (and thus low Mach number) flow of the evaporating gas, and possible hydrodynamic effects that may arise in the system are neglected. McKee & Cowie (1975) have analyzed the evaporation process in terms of a conduction front advancing into the cooler gas. They outlined an interesting analogy with the ionization fronts, and, just as in that case, the velocity of the front v_{cond} must be less than $0.5c_c^2/c_w$ (D-type front) or greater than $2c_w$ (R-type front), where c_w is the sound speed of the hot gas, and c_c is the sound speed of the cloud. In the case of an evaporating cloud, Cowie & McKee (1977) have shown that $v_{\text{cond}} \sim 2\sigma_0 c_c^2/c_w$ for classical evaporation. Thus a critical value $\sigma_{0,\text{cr}} = 0.25$ exists beyond which the conduction fronts are D-critical, and dynamical effects are important. Saturated evaporation fronts, instead, have $v_{\text{cond}} \sim 1.12\sigma_0^{1/8} c_c^2/c_w$ and are always D-critical. In this case the hot pressurized gas behind the front expands, driving a shock wave which propagates through the cold gas ahead of the conduction front itself.

The above conclusions apply under the assumption that radiative losses are negligible. If such losses exceed the conductive heat input, material condenses onto the cloud instead of evaporating. However, McKee & Cowie (1977) have shown that this occurs for $\sigma_0 < 0.03$, a circumstance never met in our models.

For our models RE01, RE05 and RE10 we have $\sigma_0 = 0.07$, $\sigma_0 = 8.59$ and $\sigma_0 = 68.7$, respectively. Hydrodynamic effects are thus expected to be absent in model RE01, but important in models RE05 and RE10. Actually, our simulations confirm this expectation. In model RE01 the cloud evaporates subsonically at the classical rate, without experiencing any compression. In models RE05 and RE10 shock waves develop and compress the evaporating cloud.

As we show in Section 3.3, all the models of evaporating clouds dragged by the superwind develop shock waves driven by the conduction front; we thus describe here in detail the model RE05, in order to emphasize the cloud dynamics generated by the thermal evaporation. As a result of the energy transfer by thermal conduction, the pressure at the cloud surface rises and drives two opposite flows. The evaporating gas moves outward subsonically while the inward flow is supersonic (Mach number $\mathcal{M} \gtrsim 3$) and drives a shock wave. This different behavior is tied to the large temperature difference between the cloud and the hot gas, and the resulting difference in the sound speeds: $c_w/c_c = 22.4$.

The spherical shock originating at the surface compresses the cloud as it converges toward the center. The evolution of model RE05 is illustrated in Fig. 2, where the cloud center is located at $r = 0$. The first two panels of Fig. 2 show the cloud evolution at $t = 0.2 \text{ Myr}$ and $t = 0.4 \text{ Myr}$, when the converging shock has not yet reached the center.

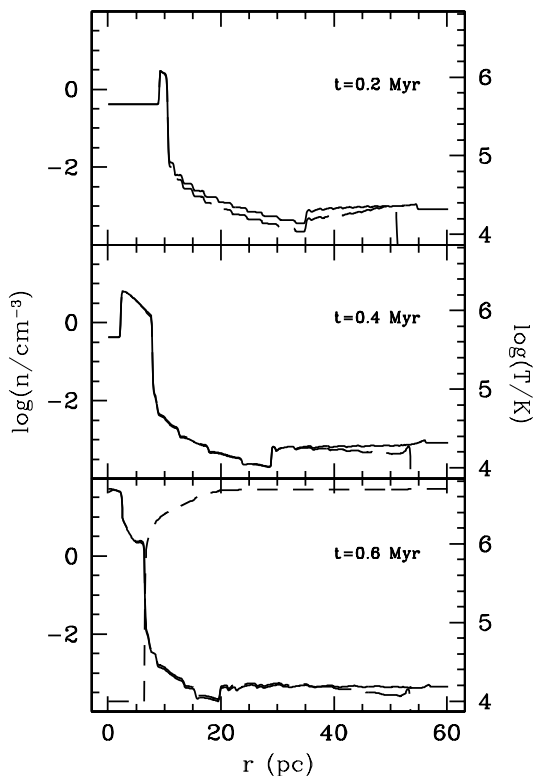


Figure 2. Density (solid line) and temperature (short dashed line) radial profiles as a function of time in the model RE05. The cloud center is located at $R = 0$, while the cloud edge was initially at $R = 15$ pc. The upper two panels show the evolution of the spherical shock induced by the thermal conduction while it is converging toward the center. The bottom panel displays the cloud structure after the shock has bounced back. The long dashed line represents the cloud gas density.

Given the strong radiative losses, the shock is isothermal. The cloud temperature remains constant because it is not allowed to cool below its initial value of 10^4 K, and thus the cloud pressure varies in pace with the cloud density. It is apparent that the post-shock density (and pressure) increases with time, as a consequence of the energy “focusing” as the wave approaches the center. This effect is expected for an converging adiabatic shock (e.g. Landau & Lifshitz 1987), but remains valid also for a radiative shock, at least in the parameters range of our models.

It is also evident that the density at the outer edge of the compressed shell, where the conduction front is located, decreases despite the overall compression of the cloud. In fact, given the negative value of the radial pressure gradient, with time the tail of the density profile lags more and more behind; the outer layers of the cloud progressively retard their collapse, and possibly revert their motion into an expansion. The density decrease at the conduction front strongly influences the evolution of OVI and X-ray cloud luminosities, as discussed in Section 3.1.1.

At $t = 0.43$ Myr the shock reaches the center and bounces back, re-expanding through the gas still moving to-

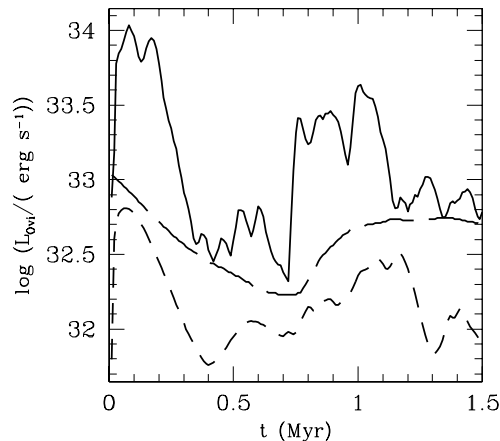


Figure 3. Time evolution of L_{OVI} (solid line) and L_X (dashed line) for the RE05 model. The cloud surface area R_c^2 is also shown in arbitrary units (long dashed line).

ward the center. At this time the central density reaches $n \sim 2.1 \times 10^3 \text{ cm}^{-3}$, nearly 5000 times larger than the initial cloud density.

The lowest panel in Fig. 2 shows the density and temperature profiles at 0.6 Myr. The density jump appearing at $r \sim 2.5$ pc indicates the position of the reflected shock. At this stage the central density of the cloud is a factor of 100 larger than the initial value. The cloud radius attains its minimum value $R_c = 5$ pc at $t \sim 0.7$ Myr, only shortly before the reflected shock reaches the edge of the cloud at $t \sim 0.75$ Myr. This latter occurrence influences greatly the cloud emission as discussed in the next subsection.

We point out that, as R_c re-expands, the thermal energy flux through the cloud surface increases as well. At $t = 0.95$ Myr, when the radius reaches the value of $R_c = 12$ pc, conditions are restored for a new collapse driven by the heat conduction. This oscillatory behaviour is not found by Ferrara & Shchekinov (1993) who performed similar 1D simulations; in their models the cloud attains a steady configuration after the initial compression. The difference is due to the fact that in their models the cloud is allowed to cool to arbitrarily low temperatures, whereas we impose a minimum temperature to approximate photo-ionization heating from massive stars.

3.1.1 OVI and X-ray emission in RE models

As a gas element evaporates from the cloud, it quickly goes through a large interval of temperatures, ranging from $T \sim 3 \times 10^5$ K where the OVI emission peaks, up to X-ray temperatures (several 10^6 K). Thus significant OVI and X-ray emission originates close to the cloud surface, and both are spatially connected. For this reason the time evolution of L_{OVI} and L_X are coupled to the cloud dynamics, in particular to the variations of the cloud density at R_c and to the evolution of the cloud size.

Both L_{OVI} and L_X have similar temporal profiles, both coarsely modulated by the behaviour of R_c . This is illustrated by Fig. 3, which shows the evolution of L_{OVI} , L_X

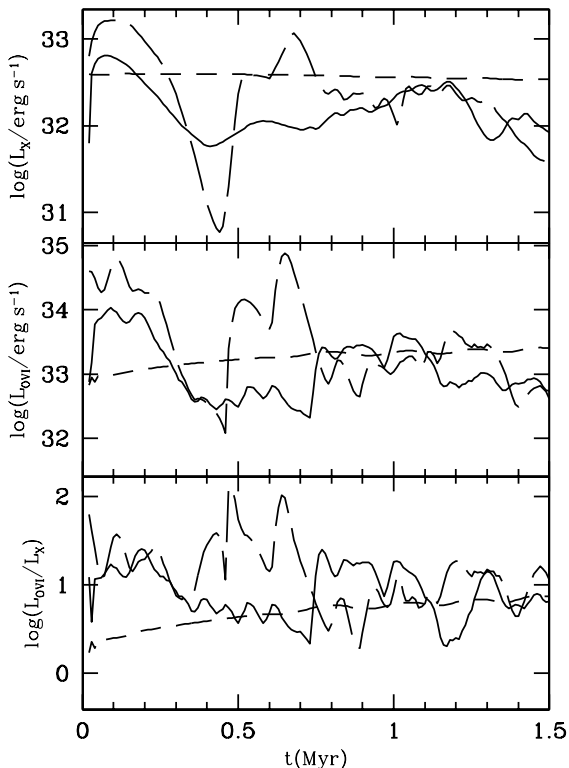


Figure 4. Time evolution of L_X (upper panel), L_{OVI} (middle panel) and $\log(L_{\text{OVI}}/L_X)$ (lower panel) for all the rest models RE. Dashed line: RE01 model; solid line RE05 model; long dashed line: RE10 model.

and R_c^2 for the model RE05. The sudden initial rise of L_{OVI} and L_X is due to the formation of the emitting layer at the cloud surface. Successively, the luminosity decreases in pace with the cloud radius; we point out, however, that the drop of L_{OVI} and L_X can not be explained only on geometrical grounds as an effect of the reduction of the emitting surface area. Fig. 3 clearly illustrates that the luminosity drop is larger than that of R_c^2 . Much of the luminosity reduction is due to a reduction of the gas density at the conduction front, a consequence of the dynamics of the imploding cloud, as previously discussed.

The sudden rise in both X-ray and OVI luminosity occurring at $t = 0.75$ Myr shown in Fig. 3 coincides with the arrival of the outwardly-propagating reflected shock at R_c . This shock compresses the gas of the emitting layer located at R_c , leading to a rapid increase in emission.

In general, the evolution of L_{OVI} and L_X is affected by a considerable “noise” due to the energy continuously injected into the cloud by the conduction front. Even if the conditions at the cloud edge are such that a strong shock can not be driven by the heat flux, density fluctuations are still generated which influence the luminosities.

The luminosities L_{OVI} and L_X of the three models RE01, RE05 and RE10 are compared in Fig. 4. In the model RE01 the dynamical effects are negligible, and the cloud suffers a steady evaporation. The rate of such evaporation is

rather low, $\dot{M} \sim 6.4 \times 10^{-6} M_\odot \text{ yr}^{-1}$, in good agreement to the analytical result presented in equation 1, and the cloud radius remains constant. The OVI flux increases slowly with time as the conduction front becomes thicker. The X-ray flux is not interesting for this model because the temperature range through the conduction front is obviously below $T_w = 10^6$, and thus no significant X-ray emission occurs at the cloud edge in this case. The constant level of L_X shown in Fig. 4 is essentially due to the surrounding hot medium.

Compared to model RE05, the oscillations of L_{OVI} and L_X are accentuated in model RE10, where the heat flux is larger because of the larger temperature gradient at the cloud edge.

In the bottom panel of Fig. 4 the ratio L_{OVI}/L_X is plotted. We will discuss how this ratio relates to the values observed in superwinds in Section 4.

3.2 Non evaporating cloud dragged by the superwind (NC models)

The interaction of a strong shock with a single cloud has been the subject of many numerical studies. In the case of non-radiative clouds a thorough analysis of this problem and a review of relevant literature is provided by Klein et al. (1994). Numerical simulations in the case of radiative clouds have been presented by Mellema et al. (2002) and Fragile et al. (2004). In all these papers, after the passage of the shock the cloud is embedded in a low-density wind, analogous to the situation considered here. However the model parameters in the papers just mentioned are not appropriate for clouds embedded in superwinds. We thus run models of non-evaporating clouds (i.e. without thermal conduction) embedded in a superwind.

The purpose of these models is twofold: on one hand they represent an useful check when compared to the results by other authors and, on the other hand, they help to understand, by comparison with analogous models with heat transfer, the role played by the conduction in the general dynamics of the cloud.

In all our models (see Table 1) the superwind is super- or-hyper-sonic (Mach number $\mathcal{M} = 3.2$ for models with low ram pressure and $\mathcal{M} = 7.1$ for models with high ram pressure), despite the high temperature assumed for the volume-filling wind material. A bow shock forms around the cloud, while a shock is driven into the cloud with velocity $v_s = v_w \chi^{-1/2}$, where $\chi = \rho_c / \rho_w$. The characteristic time τ_{cc} for the cloud to be crushed by this shock is R_c / v_s , i.e.

$$\tau_{cc} = \chi^{1/2} R_c / v_w. \quad (4)$$

This is the basic timescale governing the evolution of a cloud over-run by a blast wave or a wind, with cloud destruction expected after several crushing times (Klein et al. 1994). The cloud is fragmented by the action of both Kelvin-Helmholtz (K-H) and Rayleigh-Taylor (R-T) instabilities. The Richtmyer-Meshkov instability also contributes to the fragmentation, but it is less important because it grows linearly rather than exponentially.

The K-H instabilities are due to the relative motion between the cloud and the hot, tenuous background gas. The modes destroying the cloud are those whose wavelength is comparable to R_c , and their growth time is $\tau_{KH} \sim \tau_{cc}$ (e.g. Klein et al. 1994). This timescale estimate is a lower limit as

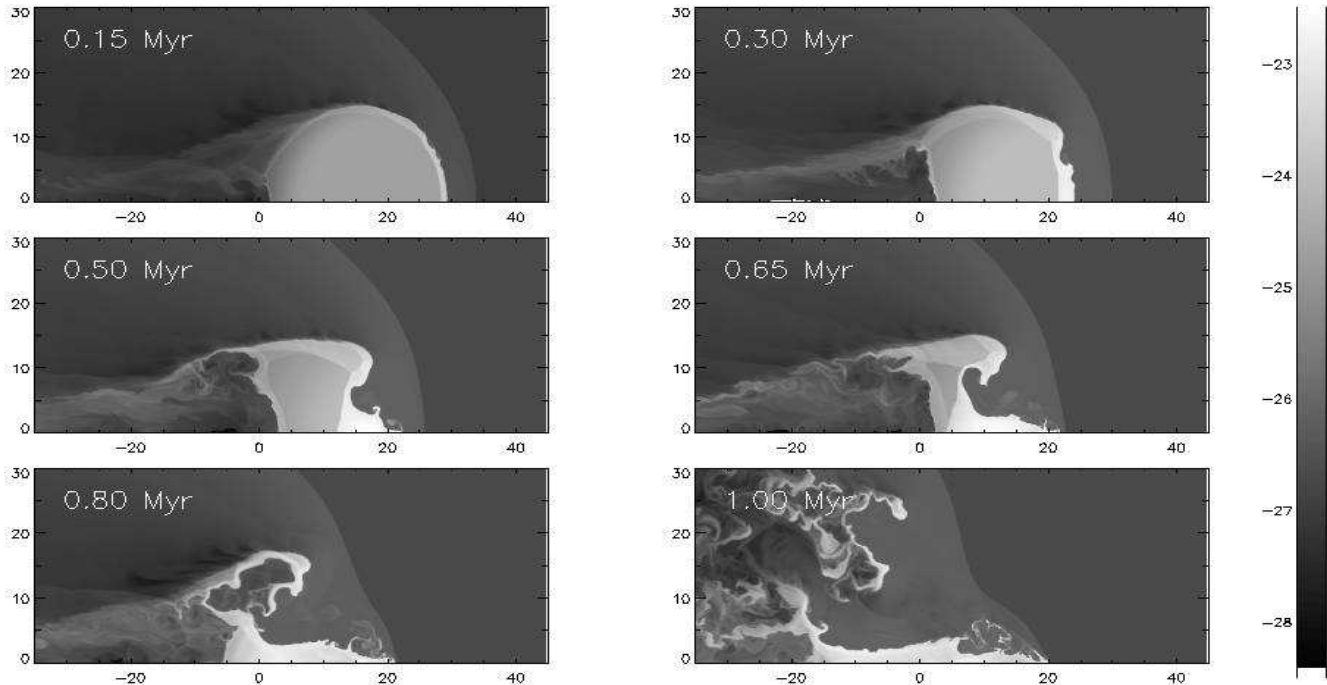


Figure 5. Density distribution at different times of the cold cloud interacting with the hot tenuous superwind for the reference model T5LPNC (no heat conduction). The logarithm of the mass density (in units of g cm^{-3}) is shown. The distances are given in pc. At the beginning of the simulation the cloud center is at $z = 20$ pc.

with the formation of the bow shock around the cloud the gas actually flowing around the cloud edge has a velocity lower than that of the unperturbed superwind.

The growth time of the R-T instability is $\tau_{\text{RT}} \sim (R_c/a)^{1/2}$, where $a \sim \pi \rho_w R_c^2 v_w^2 / M_c$ is the cloud acceleration due to the superwind ram pressure. Again, the growth time is comparable to the crushing time, $\tau_{\text{RT}} \sim \tau_{\text{cc}}$. Again the quoted timescale is a lower limit. In reality the wind attempts to form a smooth flow around the cloud, and thus the acceleration a is lower than the above estimate.

The timescales given above hold in the case of an adiabatic evolution of the gas, however they are still adequate to roughly characterize the flow in the radiative case (Fragile et al. 2004). In fact, our radiative simulations substantially confirm the picture outlined above.

In Fig. 5 we show the density evolution of the low ram pressure model T5LPNC, for which $\tau_{\text{cc}} = 3.3 \times 10^5$ yr. The perturbations grow first close to the axis of symmetry of the cloud, where the R-T instabilities are more effective. Of course K-H instabilities are also present, and the actual growth time is $\tau = (\tau_{\text{RT}}^{-2} + \tau_{\text{KH}}^{-2})^{1/2} \sim \tau_{\text{cc}}/\sqrt{2}$ (Lamb 1945). The K-H instabilities are expected to develop faster near the tangential point, where the relative velocity is larger. However, an inspection to Fig. 5 shows that this region is rather smooth; in fact the K-H modes originate at the cloud edge but grow downstream, where they are advected by the flow. For $t < t_{\text{cc}}$, while the transmitted shock is still crossing the cloud, the flow of the superwind results in a low-pressure region at the rear of the cloud, into which the cloud material moves generating a rarefaction wave which propagates into the cloud. This low-pressure region produces also a sort of

back-flow of the superwind gas, giving rise to a vortex ring responsible of the K-H instabilities which severely distort the back side of the cloud.

Although part of the cloud is highly fragmented after a few crushing times, its core remains rather compact although highly distorted. At $t = 1$ Myr the mass of the core is $47 M_{\odot}$ (the original cloud mass was $\sim 210 M_{\odot}$), while the rest of the cloud, as a consequence of the efficient radiative cooling, is leaving the grid downstream in form of dense filaments.

Our results are intermediate between those expected for a non-radiative cloud and those obtained for a radiative cloud. In the former case the cloud would either be compressed, or be completely destroyed and diffused into the ambient medium (Klein et al. 1994). The radiative cloud, instead, breaks up into numerous, dense, cold fragments which survive for many dynamical timescales (Mellema et al. 2002; Fragile et al. 2004). In our simulations the fragmentation process is present but less efficient. This is due to the fact that in our models the cloud is not allowed to cool below its initial temperature of 10^4 K, while in the papers quoted above the minimum allowed temperature is $T = 10$ K. We run a further simulation (not shown here), analogous to the reference model T5LPNC, in which the cloud is now allowed to cool down to 10 K. In this case radiative losses are more effective and the fragmentation proceeds more efficiently. The evolution is now very similar to that found in previous works of Mellema et al. (2002) and Fragile et al. (2004), and the cloud is fragmented in several small clumps after few dynamical timescale.

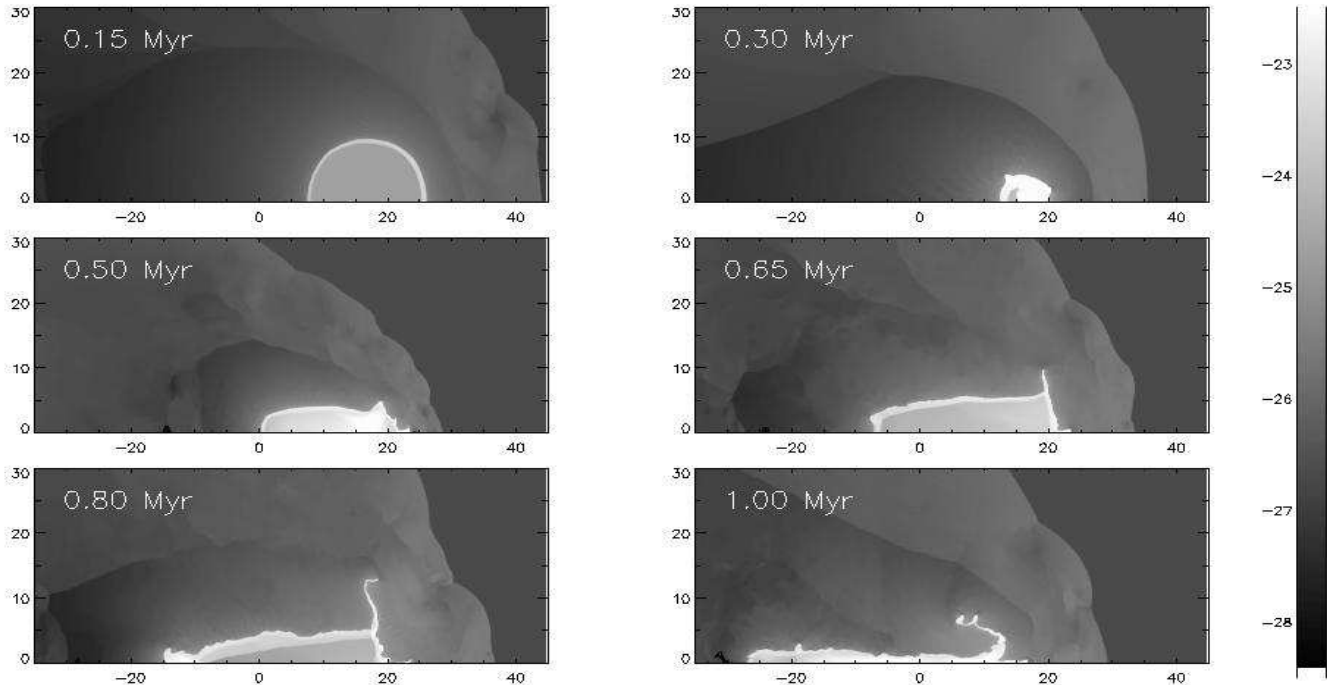


Figure 6. Density distribution at different times of the cold cloud interacting with the hot tenuous superwind for the reference model T5LP including the effects of heat conduction. The logarithm of the mass density (in units of g cm^{-3}) is shown. The distances are given in pc. At the beginning of the simulation the cloud center is at $z = 20$ pc.

3.3 Evaporating clouds dragged by the superwind

As already discussed, we found that in the RE models the dynamical effects linked to the thermal conduction become important when $\sigma_0 > \sigma_{\text{cr}}$. The post-shock gas facing the front of the cloud has a temperature $T_{\text{bs}} \sim 1.38 \times 10^7 (v_w/1000 \text{ km s}^{-1})^2$. As this temperature is always larger than the temperature T_w of the unperturbed superwind we assume, the effective initial value of σ_0 is larger than in the static case (see Table 1). In particular, σ_0 is increased above σ_{cr} also in the models T1LP and T1HP (which otherwise would have $\sigma_0 < \sigma_{\text{cr}}$), and dynamical effects due to the thermal conduction are always present in all our models of clouds within a wind.

In Fig. 6 we show the evolution of the density for the reference model T5LP. This model develops a bow shock temperature $T_{\text{bs}} \sim 1.3 \times 10^7$ K. As expected, a converging shock due to the action of the thermal conduction forms all around the cloud (see the shot at $t = 0.15$ Myr in Fig. 6), and the cloud radius has shrunk by a factor of three by $t = 0.30$ Myr. However, the shock formed at the leading edge of the cloud is stronger and moves faster through the cloud than the shock portion at the rear of the cloud. The reason for this is twofold: *i*) the temperature in front of the cloud is larger than at its backside, and *ii*) the superwind ram pressure contribution is also present at the front side. The cloud continues to collapse till ~ 0.4 Myr, when the central core reaches a pressure high enough to stop the shrinking. At this time the cloud re-expands. The expansion occurs preferentially downstream, where it is not contrasted by the ram pressure of the incoming superwind. With time the cloud loses completely its initial shape and assumes an

elongated aspect. A successive compression starts at ~ 0.75 Myr. However, given the complicated cloud morphology and the complexity of the flow, the cloud compression is not uniform, but different regions shrink at different rates (see panel of Fig. 6 at $t = 0.8$ Myr). After 1 Myr the cloud assumes a filamentary shape along the symmetry axis.

It is worth noting that, contrary to the same model without conduction, the cloud does not fragment because the R-T and K-H instabilities are strongly inhibited by the thermal conduction. The K-H instability depends on the steepness of the density and velocity gradients across the cloud surface. Since heat conduction smoothes out these gradients, the growth of the instabilities is reduced (Vieser & Hensler 2000). Furthermore the compression of the cloud due to the heat conduction reduces the momentum transfer from the superwind to the cloud, and thus the cloud acceleration responsible of the R-T instabilities.

In Fig. 7 the evolution of the mass of the cloud and the evaporation rate \dot{M} are plotted for all the models with conduction. This rate is measured by calculating the remaining cold gas mass at each simulation time step, specifically the mass of gas with $T < 1.2 \times 10^4$ K. In the non-conductive models the cloud is always heavily shredded, which makes it difficult to measure cloud mass loss, but relatively little cold gas gets heated to $T > 1.2 \times 10^4$ K. Focusing on model T5LP, at the beginning the value of the mass loss rate is in agreement with equation 3 once the temperature and density of the superwind behind the bow-shock is taken into account. As expected, the rate drops by a factor of 20 after $t = 0.35$ Myr, consistently with the analogous reduction of the evaporating surface area proportional to R_c^2 . Then

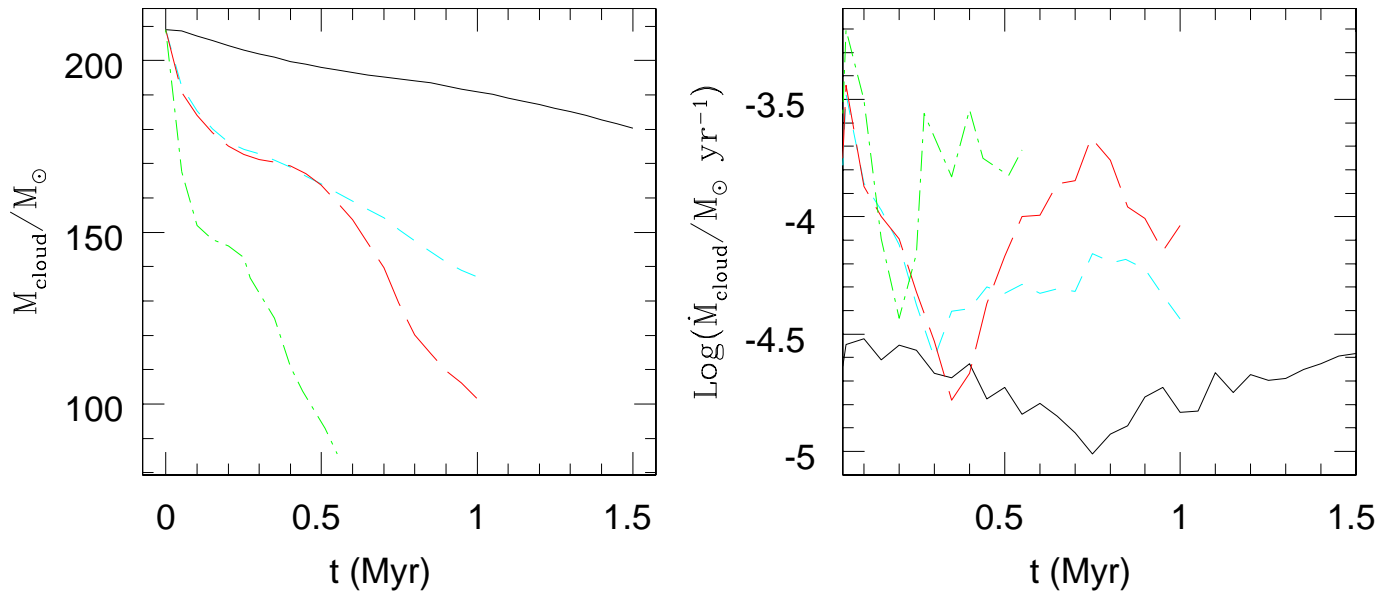


Figure 7. Mass evolution (left panel) and mass loss rate (right panel) for the evaporating cloud models. Black solid lines : T1LP; blue short dashed: T1HP; red long dashed: T5LP; green dot dashed: T5HP.

it increases again following an oscillatory behaviour in pace with the evolution of the cloud surface. The reduction of \dot{M} is reflected in the evolution of the cloud mass which shows a “flex” in its temporal profile corresponding to the minimum of the mass loss rate. The cloud lifetime turns out to be 2-3 times longer than that provided by the constant rate \dot{M} given by equation 3.

The behaviour of all the other models is qualitatively similar to that of the reference model. The right panel in Fig. 7 reveals that the evaporative mass loss rate is initially higher in models with larger values of v_w . The same models also show a larger frequency in the oscillatory behaviour of \dot{M} . Larger values of v_w lead to larger values of T_{bs} and of the heat flux. The larger the heat flux is, the faster the transmitted shock moves into the cloud; as a consequence, the re-expansion occurs earlier in models with larger v_w . The similarity of the mass loss history for models with the same v_w (at least as long as the clouds maintain a rough spherical shape) is rather striking when one compares the temporal profiles of M_c for models T5LP and T1HP (see the left panel of Fig. 7).

3.4 X-ray and OVI emission

3.4.1 OVI and X-ray emission in NC models

As pointed out in Section 3.1 when discussing clouds in a static hot medium, the interface between the cold dense cloud and the hot tenuous wind material is the source of both OVI and soft X-ray emission. In the simulations without heat conduction these two phases tend to mix at the contact surface by numerical diffusion (see Fig. 8). While such diffusion can mimic qualitatively real phenomena like molecular diffusion and turbulent mixing, the quantitative

effect can be easily overestimated giving rise to excessive radiative losses and overly-rapid cloud destruction.

It has been argued that the numerical spread of the contact discontinuities could in principle simulate, at least qualitatively, the presence of a heat conduction front; such an analogy, however, may be grossly in error in all the cases in which the conduction front is expected to give rise to dynamical effects such those described in the previous section, and which can not be generated by numerical diffusion. As shown in the previous section the inclusion of the thermal conduction significantly alters the dynamical behavior of the cloud. We also find that the radiative characteristics of the cloud change significantly.

In Fig. 8 we plot the evolution of the OVI and X-ray volume emissivity (i.e. luminosity per unit volume, $n_e n_H \Lambda(T)$) as a function of time for the reference model T5LPNC. In the left hand side panels of Fig. 9 the OVI and X-ray luminosities, and X-ray luminosity-weighted wind mass fraction $\langle \mathcal{R} \rangle$ of all the non-conductive models are compared.

The OVI luminosity in model T5LP increases exponentially during the first $\sim 2.4\tau_{cc} \sim 0.8$ Myr (see Fig. 9), when the cloud, although highly distorted, is not yet fragmented. The rise in L_{OVI} is due to the increase of the emitting surface area of the cloud. Subsequently the increase in L_{OVI} is even more substantial as cloud fragmentation increases the cumulative emitting surface. Finally, after $t \sim 1.2$ Myr, the L_{OVI} measured within the simulation volume drops as the cloudlets (which are more easily accelerated by the wind) start to leave the computational grid.

Soft X-ray emission originates not only at the cloudlets’ surfaces but also in the region behind the bow shock, where the temperature is $T \sim 1.6 \times 10^7$ K and the density $\sim 2.6 \times 10^{-3} \text{ cm}^{-3}$. Wind-based material dominates the X-ray emission at times $t \lesssim 0.8$ Myr, based on the X-ray luminosity weighted wind mass fraction \mathcal{R} (bottom left panel of

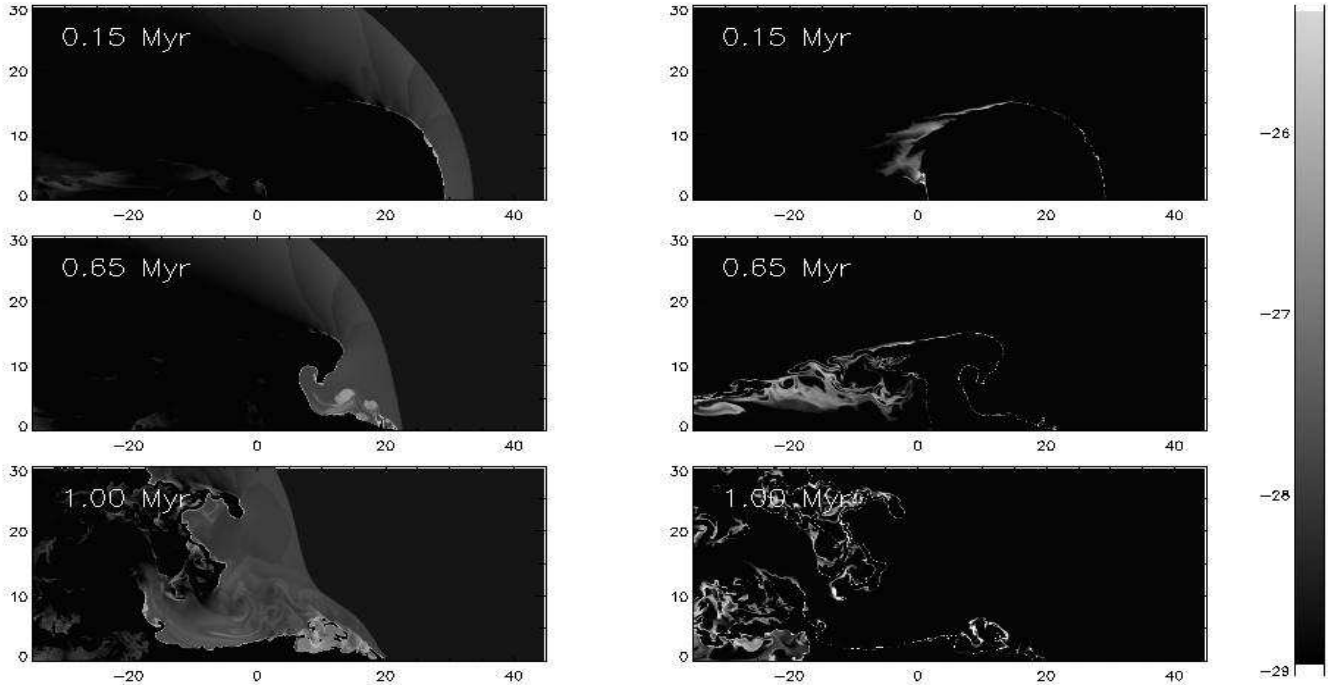


Figure 8. X-ray (left panels) and OVI (right panels) volume emissivity for the reference model T5LPNC at the same times of Fig. 5. The logarithm of the soft X-ray (0.3 – 2.0 keV energy band) and OVI volume emissivity (in units of $\text{erg s}^{-1} \text{cm}^{-3}$) is shown.

Fig. 9). Once fragmentation becomes significant at $t \gtrsim 0.8$ Myr the fraction of emission from cloud material increases to a maximum of $\sim 60\%$. It is worth noting that in Fig. 9 the contribution of the X-ray background due to the unperturbed hot superwind is also present. This contribution is of the same order of magnitude of that of the cloud, and this explains the rather low increase of L_X during the first 0.8 Myr. Later, analogous to case of L_{OVI} , the X-ray luminosity shows a rise and fall due to cloud fragmentation and loss of cloudlets from the computational grid.

Model T1LPNC has the same ram pressure and the same analytical crushing timescale τ_{cc} of the model T5LPNC just discussed, but lower superwind velocity and lower cloud to wind density ratio of $\chi = 100$. As pointed out by Klein et al. (1994), the time at which the cloud substantially fragments is also inversely proportional to χ . This is confirmed by our simulations in which the model T1LPNC fragments less dramatically than the model T5LPNC. This different dynamical behaviour is responsible for the different time evolution of L_{OVI} in model T1LPNC, which increases at lower rate and, in particular, does not show the “bump” present in the reference model associated to the occurrence of the strong fragmentation. Note that the initial value of L_{OVI} in model T1LPNC is larger than in model T5LPNC because of the different background contribution by the superwind. The X-ray luminosity in model T1LPNC is always dominated by the emission from wind material in the region behind the bow shock (\mathcal{R} is always ~ 1). Here the gas has a temperature $T \sim 3 \times 10^6$ K and a number density of $\sim 1.3 \times 10^{-2} \text{cm}^{-3}$. The density is nearly five times larger than in the reference model, and thus L_X is also larger.

Going back to the high ram pressure models T1HPNC

and T5HPNC, qualitatively the temporal evolution of L_{OVI} and L_X is similar to the low pressure models, although occurring on shorter timescales. This is as expected as for both T1HPNC and T5HPNC $\tau_{\text{cc}} = 1.5 \times 10^5$ Myr, shorter than in the models with lower ram pressure. The increase in L_{OVI} occurs at earlier times because of the faster fragmentation, and is higher in magnitude in model T5HPNC because of its higher value of χ , as discussed above. The strong luminosity drop occurring at $t = 0.5$ Myr is again due to the fact that the cloud fragments leave the computational grid. The luminosity peak due to the fragmentation is also present in the X-ray luminosities, and is associated with a drop in the fraction of the emission due to wind material. Given the larger superwind density in model T1HPNC the bow-shock is of relatively greater importance in this model, and the relative rise in L_X associated with cloud fragmentation is smaller than in T5LPNC or T5HPNC.

3.4.2 OVI and X-ray emission of evaporating clouds dragged by the superwind

Fig. 10 shows the OVI and X-ray emissivity maps of the reference model T5LP at different times. As in the models without heat conduction, the X-ray flux originates not only close to the cloud surface, but also behind the bow-shock. The X-ray and OVI volume emissivity is largest at the leading edge of the cloud, close to the symmetry axis, where the density of the evaporating gas has a maximum. This is due in part to the larger temperature of the shocked superwind, and partially to the compression given by the ram pressure.

In Fig. 9 (right panels) we plot the time evolution of L_X , L_{OVI} , L_{OVI}/L_X and \mathcal{R} for all the models with thermal

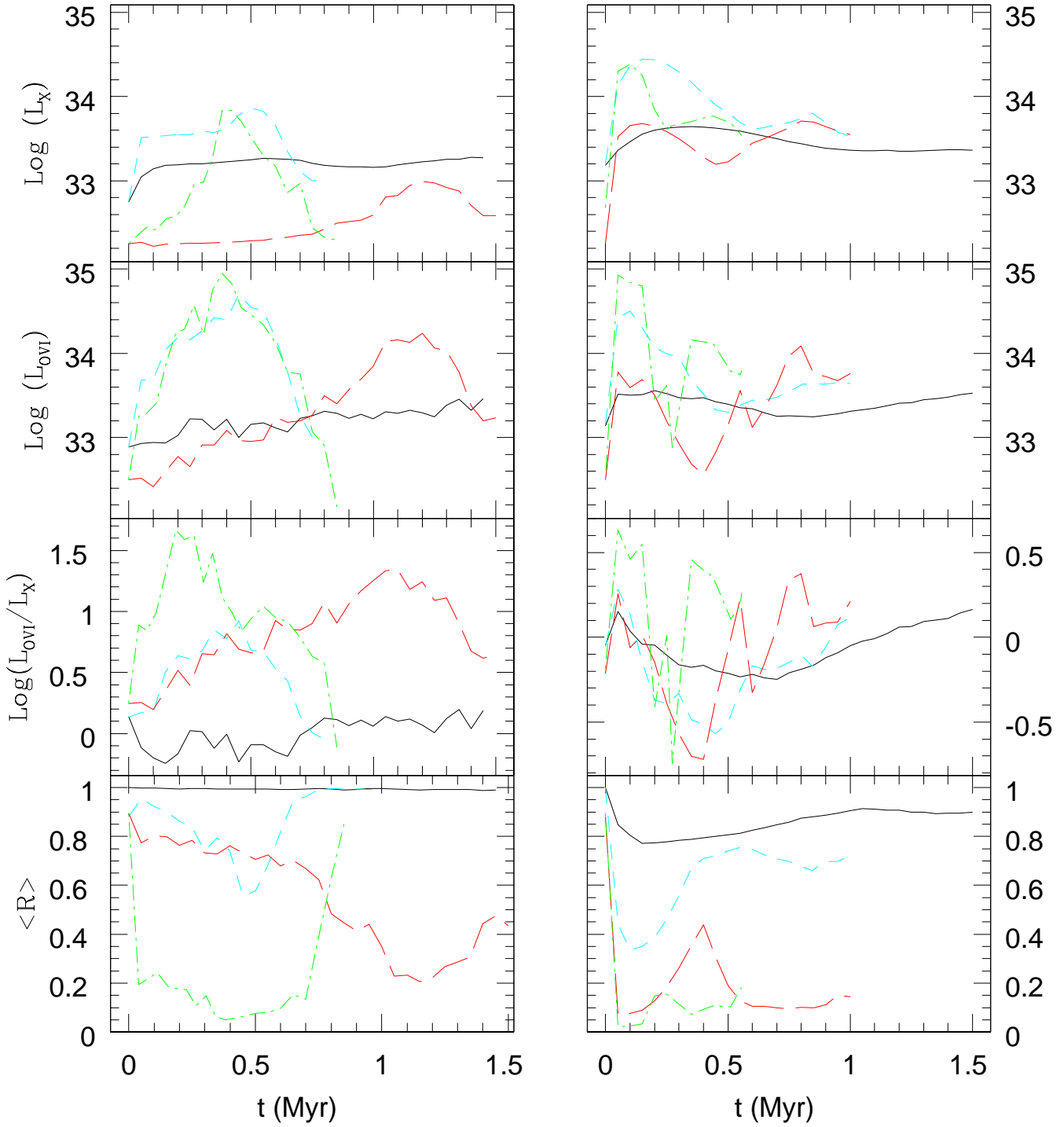


Figure 9. Time evolution of the logarithm of X-ray (top panel) OVI (second panel down) luminosities and the logarithm of their ratio (third panel down) and X-ray luminosity-weighted wind mass fraction $\langle \mathcal{R} \rangle$ for all models. The right panels refer to models with the inclusion of effects due to heat conduction, while left panels refer to non-evaporative models NC. Black solid lines: T1LP; blue short dashed: T1HP; red long dashed: T5LP; green dot dashed: T5HP.

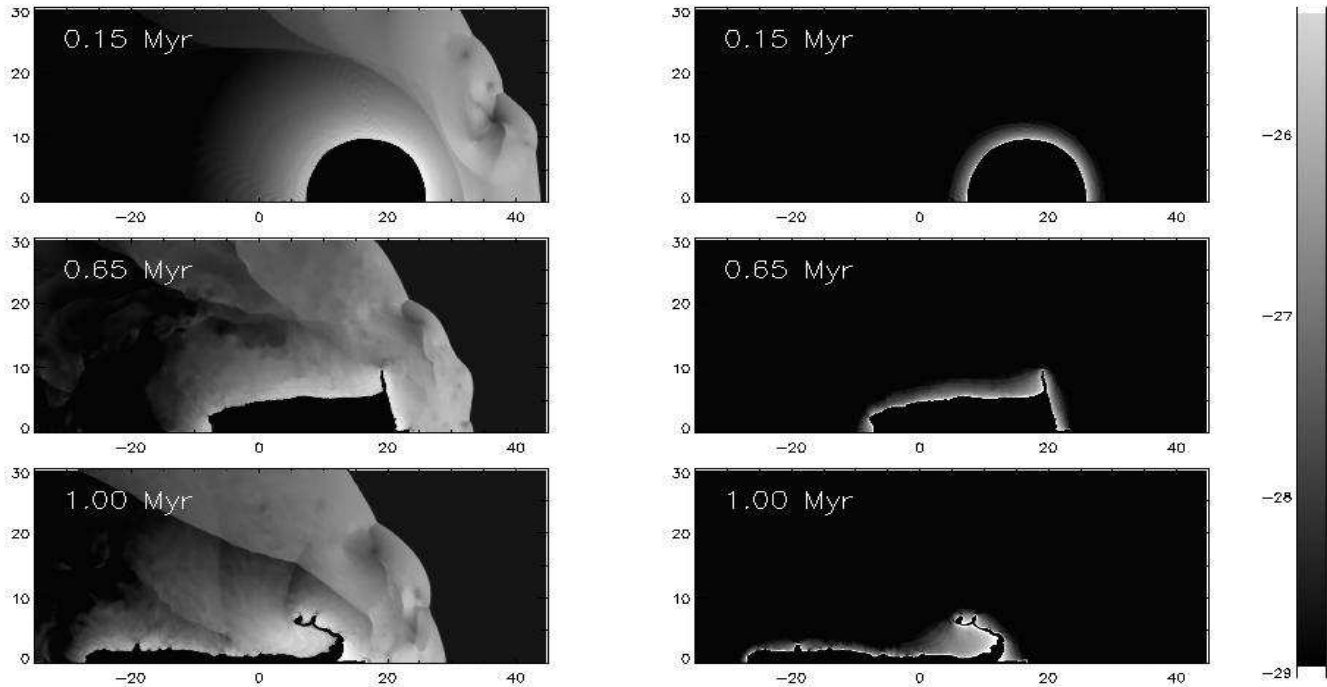


Figure 10. X-ray (left panels) and OVI (right panels) volume emissivity for the reference model T5LP at the same times of Fig. 6. The logarithm of the soft X-ray (0.3 – 2.0 keV energy band) and OVI volume emissivity (in units of $\text{erg s}^{-1} \text{cm}^{-3}$) is shown.

conduction. Concentrating in particular on model T5LP, the OVI and soft X-ray luminosities follow the same oscillating behaviour seen in mass loss rates of the cloud (Fig. 7), and are similar to the analogous model at rest (see e.g. Fig. 4). Note that now the luminosities are systematically higher than in model RE05, and are more similar to those in model RE10. This is due to the larger evaporating flux of emitting gas due to the higher bow shock temperatures, as outlined above. The low values of \mathcal{R} demonstrate that the X-ray emission is now dominated by cloud material at essentially all times (at least in this case where $Z_w = Z_c$) When compared with the T5LPNC model (left hand side panels of Fig. 9), both L_X and L_{OVI} are, at least at early times, up to 15–25 times higher than the values of the same model without conduction.

The L_{OVI}/L_X ratio in these models is lower than in either the static conductive models, or in the non-conductive wind models. This is due to the combined effect of the heat conduction and of the bow shock, which tends to increase the X-ray flux more than the OVI flux. It is only in model T1LP that conduction does not significantly increase the X-ray emission from the wind/cloud interaction. In all other conductive models X-ray luminosities are higher, and a larger and often dominant fraction of the emission comes from material that was originally part of the cloud.

The time evolution of the luminosities of the other conductive models is similar to that of the reference model T5LP (see Fig. 9), and the relative differences in the oscillating period grossly follow the analogous differences found in the behaviour of \dot{M} (see Fig. 7). In general, the amplitudes of the luminosity fluctuations are larger for models with larger values of T_{bs} , and thus larger evaporative \dot{M} .

Note, however, that the luminosities in model T1HP reach higher values than in model T5LP although this latter develops essentially the same mass loss in the first 0.5 Myr. This is a consequence of the larger value of the ram pressure which reduces the volume between the cloud and the bow shock. This is the region where the volume emissivities are largest, and where the evaporating gas in the front edge of the cloud moves before to be dragged downstream. The increase in the mean density of this region due to the reduced volume behind the bow shock thus leads to higher luminosities.

3.5 OVI absorption line column densities and kinematics

In addition to calculating the X-ray and OVI emission from these models we also consider absorption line properties, specifically column densities of the OVI ion probed in FUSE observations of starbursts (see e.g. Heckman et al. 2001b, 2002).

Most of the physical and dynamical effects that alter the previously-discussed X-ray and OVI emission also affect the gas that would be seen with absorption line probes. We have therefore kept this discussion short, and present only the time-averaged OVI column densities for each of the models in Table 4. For each model we report the mean value of N_{OVI} through the center of the cloud averaged over two different radii: $R_{\text{sor}} = 5 \text{ pc}$ and $R_{\text{sor}} = 15 \text{ pc}$ (this latter being equal to the cloud radius). Note that these radii give rise to a spatial area lower than that subtended by a FUSE LWRS aperture.

Thus, if the areal covering fraction of clouds within an

Table 3. Mean fractions of wind mechanical energy radiated and L_{OVI}/L_X ratios in the wind/cloud interaction, and in the undisturbed wind.

Model	L_{mec} erg s ⁻¹	$\langle L_X/L_{\text{mec}} \rangle$ (%)	$\langle L_{\text{OVI}}/L_{\text{mec}} \rangle$ (%)	$\langle L_{\text{tot}}/L_{\text{mec}} \rangle$ (%)	$\langle L_{\text{OVI}}/L_X \rangle$ ($Z_w = Z_\odot$) (6) (7)		t_{avg} Myr
(1)	(2)	(3)	(4)	(5)	(6)	(7)	(8)
T1LP(NC)	1.34×10^{36}	0.23 (0.122)	0.20 (0.13)	0.89 (0.55)	0.87 (1.07)	0.1 (0.11)	1.5 (1.5)
...	...	0.045	0.028	0.138	0.62	0.62	...
T1HP(NC)	1.50×10^{37}	0.07 (0.002)	0.05 (0.11)	0.25 (0.37)	0.71 (44.5)	0.12 (5.23)	1.0 (0.8)
...	...	0.0040	0.0025	0.0123	0.62	0.62	...
T5LP(NC)	3.00×10^{36}	0.12 (0.013)	0.13 (0.14)	0.55 (0.49)	1.11 (11.2)	0.34 (1.68)	1.0 (1.5)
...	...	0.0062	9.7×10^{-7}	0.0062	1.6×10^{-4}	1.6×10^{-4}	...
T5HP(NC)	3.33×10^{37}	0.03 (0.004)	0.07 (0.08)	0.29 (0.26)	2.68 (18.5)	1.31 (7.58)	0.55 (0.8)
...	...	0.00056	8.8×10^{-8}	0.00056	1.6×10^{-4}	1.6×10^{-4}	...

Notes — The time-averaged mean X-ray, OVI and total luminosities are given as a fraction of the superwind mechanical power $L_{\text{mec}} = 0.5 \rho_w v_w^3 \pi R_{\text{em}}^2$ passing through the chosen volume (a cylinder of radius $R = 10$ pc and extending 20 pc upstream and 80 pc downstream of the initial cloud center). Note that the luminosities are calculated over a larger volume, with a radius of 50 pc. See Section 4.4 for details. Columns are as follows: Column 1: Model name. Values given in parentheses correspond the cloud models without thermal conduction. The second line of values associated with each model shows the L_X/L_{mec} , $L_{\text{OVI}}/L_{\text{mec}}$, $L_{\text{tot}}/L_{\text{mec}}$ and L_{OVI}/L_X values for an equal volume of wind material with no clouds within it. Column 2: Wind mechanical luminosity L_{mec} . Column 3: Average soft X-ray emission (E=0.3-2.0 keV) to wind mechanical power ratio (in percent). All values in columns 3 – 6 were calculated using $Z_w = Z_c = Z_\odot$. Column 4: Average OVI doublet ($\lambda = 1032 \text{ \AA}$ and 1038 \AA) emission to wind mechanical power ratio (in percent). Column 5: Average total FUV and soft X-ray emission to wind mechanical power ratio (in percent), assuming the Ovi emission accounts for 30% off the total FUV cooling rate (Hoopes et al. 2003). Column 6: Average OVI to soft X-ray luminosity ratio. Column 7: As column 6, except calculated with $Z_c = Z_\odot$ and $Z_w = 10Z_\odot$. Column 8: The time over which the luminosities were averaged.

LWRS is of order unity, then this is the column density that would be observed. But, if the cloud covering factor is less, then the column density that would be observed with the LWRS on FUSE would be proportionally less.

In the models without conduction the OVI column density N_{OVI} varies with time, depending on the fragmentation of the cloud, and roughly proportional to the behaviour of L_{OVI} . From Table 4 it is clear that the time-averaged mean column density $\langle N_{\text{OVI}} \rangle$ is higher for models with larger wind ram pressure (and consequently shorter cloud crushing time τ_{cc}). Models with the same ram pressure have roughly the same value of N_{OVI} (within 0.1 dex). Analogously to our earlier discussion on the L_{OVI} behaviour, the model T5LPNC has a slightly higher mean N_{OVI} value compared to equivalent ram pressure model T1LPNC, most probably because of the higher cloud fragmentation (which depends on the cloud density contrast χ). An effect of similar magnitude is seen comparing the non-conductive high pressure models.

These effects are most clearly seen along lines of sight weighted toward the center of the original cloud where the density of $T \sim 10^{5.5}$ K gas is greatest, i.e. $R_{\text{sor}} = 5$ pc in Table 4. Mean density columns over a larger radius still show the same general pattern in these non-conductive models, as cool clouds fragment and their OVI interfaces extend to radii greater than that of the original cloud.

The inclusion of thermal conduction alters the mean OVI columns as follows. Conductive effects crush the cloud, and cloud fragmentation is almost completely suppressed. As a result there is a large difference between the mean N_{OVI} column density averaged over a line of sight of 5 pc radius (which always intersects the cloud) to that averaged over 15 pc radius (which often includes line of sight with negligible OVI-absorbing material).

Considering $R_{\text{sor}} = 5$ pc, the $\langle N_{\text{OVI}} \rangle$ value observed

is physically driven by the bow shock temperature T_{bs} (as is the case for L_{OVI}), with higher T_{bs} driving more conductive evaporation and hence creating more $T \sim 10^{5.5}$ K gas. Note how much closer the N_{OVI} values are between models T1HP and T5LP (which have very similar post-shock temperatures T_{bs}) than in the case of the equivalent non-conductive models. The higher N_{OVI} value for T5LP is due to the higher initial temperature of the wind in T5LP. This hotter gas also drives stronger evaporation behind the cloud (on the reverse side to the wind bow shock) than in model T1HP.

When averaging the OVI column over the larger radius of $R_{\text{sor}} = 15$ pc, the time-averaged N_{OVI} is relatively uniform, even slightly decreasing as T_{bs} increases. Here the strong increase in N_{OVI} with increased T_{bs} along lines of sight passing through the cloud is offset by increased numbers of lines of sight with negligible N_{OVI} , as increased T_{BS} leads to stronger cloud compression and reduces its cross-section.

Within the short period of time over which we can follow the evolution of the cloud in these simulations the cold gas is accelerated by the wind to a mass-weighted average velocity between 20 and 100 km s⁻¹ (at $t = 0.5$ Myr). Cold gas velocities are systematically larger in the high ram pressure models compared to low pressure models. Comparing equivalent conductive and non-conductive models, the mean cold gas velocity is higher in the non-conductive models as cloud fragments are easily accelerated to higher velocity. The fraction of the wind mechanical energy converted to cloud kinetic energy by this time (calculated within a radius of 10 pc for all models) ranges between 0.6 and 6%, and on average is 2% for models with conduction and 5% for non-conductive models. Note that more wind mechanical energy is converted to cloud kinetic energy than is radiated away (see Table 3).

We investigated the OVI kinematics of a randomly-

chosen subsample of the simulated OVI absorption lines. Mean velocities were in the range 0 to 200 km s⁻¹, although we did not find any clear correlation between mean cold gas velocities and OVI profile velocities. We found line widths equivalent to b values in the range 30 to 200 km s⁻¹.

3.6 The influence of the cloud radius

In all the previously described simulations, the initial radius of the cool cloud was 15 pc, consistent with the smallest scale structures observed in the warm ionized gas in superwinds and seen in numerical simulations of superwinds (as discussed in Section 1). This does not mean that cool clouds of only this size exist. Much larger structures of relatively cool $T \lesssim 10^4$ K gas exist (e.g. the northern cloud or cap in M82, see Lehnert et al. 1999, or the large scale filaments in the halo of NGC 253) although how coherent these structures are is hard to assess, and these very large structures may actually mark to edges of the flow rather than being fully embedded within the wind.

The distribution of cloud sizes and masses in winds has not been determined observationally or theoretically. As the average cloud size may differ from the $R_c = 15$ pc used as a default in our simulations it is worth considering how the emission and absorption properties of a superwind/cloud interaction depend on cloud radius. To investigate this we ran one further model, with a cloud of radius $R_c = 45$ pc (three times larger than in all the previously discussed models), on a grid with resolution $\Delta r = \Delta z = 0.3$ pc. All other model parameters were the same as in the low pressure conductive model T1LP.

We compared the soft X-ray luminosity, OVI luminosity and time-averaged OVI column density in this large radius model to the values found in model T1LP, after subtracting the background due to the undisturbed superwind within the same volume. As described in Section 2, for the model with $R_c = 15$ pc the soft X-ray and OVI emission was calculated within a radius of 50 pc off the cloud axis, and 20 pc upstream and 80 pc downstream of the initial location of the cloud. As this is similar to the size of the cloud in the larger cloud radius model we also calculated the *emission* from the large cloud radius model within a region 3 times larger in each dimension than that used in the default models. Column densities were calculated within the same 5 and 15 pc radii, but along a path length 3 times larger. As the size of regions used differ between the default model and the large cloud radius model, we subtracted the emission or absorption contribution expected from the undisturbed wind within the region to allow a fair, if approximate, comparison of the relative change in luminosity or column density.

The soft X-ray emission in the large cloud radius model is ~ 40 times greater than in model T1LP, i.e. scaling roughly as $L_X \propto R_c^{3.3}$. As the soft X-ray emission in this supersonic wind/cloud interaction mainly arises in the bow shock (in model T1LP conduction plays less of a role in enhancing the X-ray emission than in the other conductive model), this scaling can be understood as cross section of the bow shock scaling as R_c^2 and its thickness scaling as R_c^1 , and thus the luminosity scales as the approximate increase in shocked gas volume.

In contrast to the X-ray emission, which is spread over a large volume within the bow shock, the OVI emission is

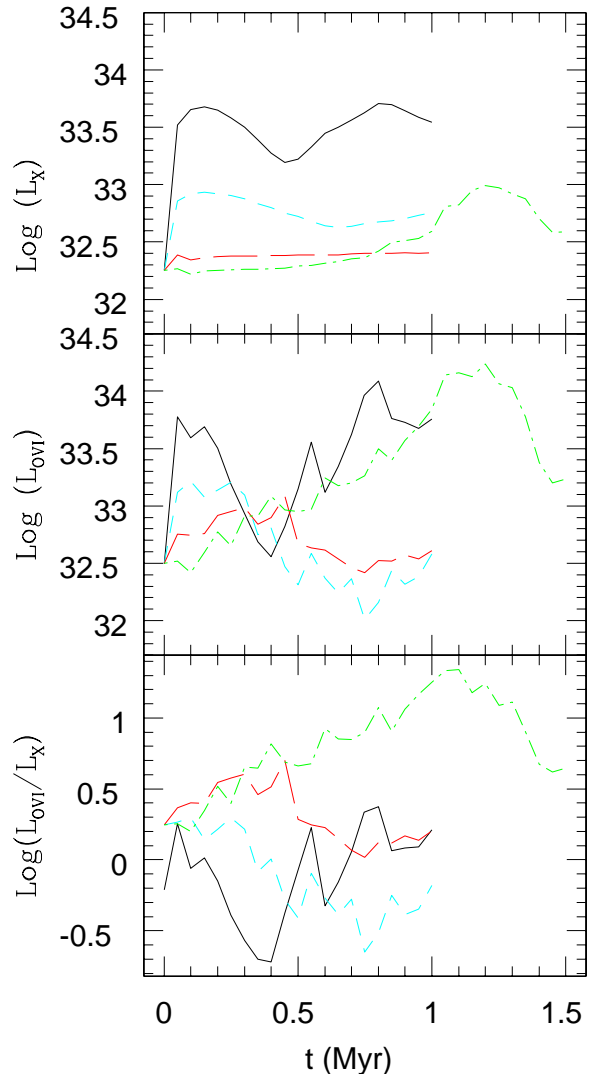


Figure 11. Time evolution of the logarithm of the X-ray (upper panel), OVI (middle panel) and the logarithm of their ratio (bottom panel) for model T5LP for different values of the reduction factor f of the Spitzer heat conduction coefficient. Black solid line: $f = 1$; blue short dashed: $f = 5$; red long dashed: $f = 25$; green dot dashed: $f = \infty$.

concentrated onto a relatively thin interface region at the immediate edge of the cloud core. The relative increase in L_{OVI} is only a factor ~ 12 , which indicates that $L_{\text{OVI}} \propto R_c^2$. This suggests that the thickness of OVI zone of the conductive front is relatively independent of the cloud radius (to within $\sim 30\%$), and that most of the OVI luminosity increase is due to increased cloud surface area.

This conclusion is supported by the simulated OVI column densities, which are very similar between the large cloud radius model and model T1LP. For the large cloud radius model the time averaged mean is $\log N_{\text{OVI}} = 12.89$ for $R_{\text{sor}} = 5$ pc (higher by $\sim 7\%$), and $\log N_{\text{OVI}} = 13.11$ for $R_{\text{sor}} = 15$ pc (higher by $\sim 70\%$). As in model T1LP the cloud is compressed to radii less than 15 pc so that some lines of sight see little or no OVI-absorbing gas, the fairest

Table 4. Mean OVI column densities through the simulated clouds.

Model	log (N_{OVI})		Model	log (N_{OVI})	
	$R_{\text{sor}} = 5$ pc	$R_{\text{sor}} = 15$ pc		$R_{\text{sor}} = 5$ pc	$R_{\text{sor}} = 15$ pc
T1LP	12.86	12.88	T1LPNC	13.08	12.54
T1HP	13.29	12.83	T1HPNC	13.29	12.98
T5LP	13.43	12.80	T5LPNC	13.19	12.97
T5HP	13.52	12.80	T5HPNC	13.38	13.05

Notes — Time-averaged mean values of $\log N_{\text{OVI}}$ (in units of cm^{-2}) due to the wind/cloud interaction in each of the models. See Section 3.5 for details. The OVI column density due to the undisturbed wind within the computational volume has been evaluated and subtracted from the total derived OVI column density, i.e. the quoted column density is the additional OVI column generated by the wind/cloud interaction. The undisturbed wind has $\log N_{\text{OVI}} = 12.65$ in all T1 models, and $\log N_{\text{OVI}} = 10.04$ in all T5 models.

comparison is between the columns averaged over the $R = 5$ synthetic beam. The similarity in column density is thus consistent with a conductive interface whose density and thickness is independent of the cloud radius to first order.

Thus these results indicate that important emission properties, specifically the soft X-ray emission, but also the related L_{OVI}/L_X ratio and the fraction of wind energy lost to radiation (L_X/L_{mec} and $L_{\text{tot}}/L_{\text{mec}}$), do depend on the cloud radius (larger clouds will give lower L_{OVI}/L_X ratios and higher L_X/L_{mec} ratios).

3.7 Lower values of the coefficient of thermal conductivity

Both X-ray observations of the hot inter-cluster medium (e.g. Ettori & Fabian 2000; Vikhlinin et al. 2001) and theoretical considerations (Narayan & Medvedev 2001; Asai, Fukuda, & Matsumoto 2004; Chandran & Maron 2004), suggest that the actual heat conduction coefficient is reduced in the presence of tangled magnetic fields by a factor of at least 5 relative to the Spitzer value. In order to understand how sensitive our results are to the absolute value of the conductivity coefficient κ we ran two more models analogous to model T5LP, but reducing this coefficient by factors $f = 5$ and $f = 25$ respectively, i.e. $\kappa = \kappa_{\text{Sp}}/f$, where $\kappa_{\text{Sp}} = 6.1 \times 10^{-7} T^{5/2} \text{ erg s K}^{-1} \text{ cm}^{-1}$ is the “standard” Spitzer value (adopted in Eq. 1 and in all the simulations with heat conduction discussed so far. Thus $f = 1$ represents model T5LP, and $f = \infty$ is model T5LPNC). We also ran a model with $f = 125$, but the results were very similar to those with $f = \infty$, so we do not discuss this model further.

As expected the apparent strength of the R-T and K-H instabilities increase as f increases. However, within $t = 1$ Myr (the time at which the simulations have been stopped) the cloud does not undergo any significant fragmentation even for $f = 25$. This fact influences the temporal behaviour of L_X and L_{OVI} . The upper panel of Fig. 11 illustrates L_X temporal profiles of the model T5LP for the four values of f , $f = (1, 5, 25, \infty)$. The profile for $f = 5$ is similar in shape to that for $f = 1$ but at lower X-ray luminosity because of the weaker conductive mass loading of the bow shock region. The oscillations are weaker because the reduced heat conduction produces smaller oscillations of the cloud radius.

Table 5. Mean OVI to X-ray flux ratios and OVI column densities for different values f of the reduction of the coefficient of thermal conductivity, in models based on T5LP conditions. All calculations assume $Z_w = Z_{\odot}$.

f	$\langle L_{\text{OVI}}/L_X \rangle$	log (N_{OVI})	
		$R_{\text{sor}} = 5$ pc	$R_{\text{sor}} = 15$ pc
1	1.1	13.43	12.80
5	1.0	12.39	12.04
25	2.3	12.11	12.20
∞	11.2	13.19	12.97

Notes — see Section 3.7 for details.

The X-ray luminosity for $f = 25$ is rather constant and only slightly larger than that for $f = \infty$. Note however that, for $t > 0.8$ Myr, L_X for the model T5LPNC increases because of the fragmentation, while remains nearly constant for $f = 25$. For the same reason, L_{OVI} remains quite low for $f = 5$ and $f = 25$ relative to $f = \infty$ (second panel of Fig. 11).

The cloud lifetime for these models with conduction of intermediate strength ($5 < f < 25$) is increased because of the reduced evaporation rate while the fragmentation remains essentially inhibited.

In Table 5 we summarize the time-averaged mean ratio L_{OVI}/L_X for different values of f . It is interesting to note that this value is essentially the same for values of $f = 1$ and $f = 5$, and only increases to 2.3 for $f = 25$. As shown in Fig. 11 the increase in L_{OVI}/L_X ratios with increasing f is due to the gradual reduction in L_X while L_{OVI} values are relatively similar irrespective of the strength of thermal conduction.

It is also interesting to compare the different values of the mean OVI column density for different values of f (shown in Table 5), where two values of R_{sor} are considered. For $R_{\text{sor}} = 15$ the column density is reduced by a factor of 5 as f increases from $f = 1$ to $f = 5$. This can be easily understood because the amount of the OVI emitting gas is roughly proportional to the rate of mass loss, and thus to f^{-1} . We point out that for $R_{\text{sor}} = 5$ the difference is larger because, contrary to the case $f = 1$, with $f = 5$ the cloud shrinks less and does not fit entirely inside R_{sor} . As f increases further, the column density reverts this trend and

increases again. This is due to the effect of the numerical diffusion which starts to prevail on the thermal conduction in spreading the cloud edge when $5 < f < 25$. The column density increase for $f > 25$ is due to the occurrence of the fragmentation and the subsequent increase of the emitting surface.

These results suggest that even with thermal conduction inhibited by realistic amounts the interesting dynamical and radiative effects of conduction on wind/cloud interactions are retained. X-ray emission is enhanced, the $L_{\text{OVI}}/L_{\text{X}}$ ratio remains low, and hydrodynamical cloud fragmentation is inhibited.

4 DISCUSSION AND IMPLICATIONS FOR SUPERWINDS

4.1 Cloud survival in superwinds

In order to produce the broad absorption line profiles of warm, neutral and coronal gas observed in superwinds, ambient ISM material must survive being entrained within the hotter superwind material long enough for it to be accelerated from rest to velocities of several hundred km/s (Heckman et al. 2000, 2001b; Heckman 2005). Warm ionized gas is observed to extend out to heights of $H_{\text{WIM}} \gtrsim 10$ kpc from the host galaxy in many superwinds. If this material has been transported from an original location within the disk this would imply a life time of $t \sim 2 (H_{\text{WIM}}/\text{kpc}) / (v_{\text{WIM}}/500 \text{ km s}^{-1})$ Myr. Yet clouds overrun by a blast wave or enveloped in a supersonic wind are expected to be hydrodynamically destroyed within a few crushing time scales (see Klein et al. 1994), which are typically less than 1 Myr for typical estimates of superwind and cloud parameters (see Table 1).

Understanding the conditions most conducive to cloud survival is therefore important. Theoretical models in which clouds are rapidly destroyed are also less likely to be good representations of the physics of superwinds than those in which clouds have longer lifetimes.

In this work we find that cloud models with thermal conduction have very different properties in terms of cloud survival to those without conduction. Thermal conduction suppresses the instabilities that strongly fragment the cloud in the non-conductive case, but also leads to significant cloud mass loss by evaporation into the hotter phases.

The mass and mass loss rate in cold gas ($\log T < 4.08$) is shown as a function of time in Fig. 7 for the models with thermal conduction. The majority of this mass loss is due to conductive-driven evaporation, as cold cloud gas is heated to $T \gtrsim 10^5$ K. As previously discussed in Section 3.3, the net evaporation rate is proportional to some power of the temperatures of the bow shock around the cloud, so the evaporation rate is least in the low wind velocity, low wind temperature model T1LP. The saturation of thermal conduction reduces the evaporation rates compared to the classical case (Equ. 3), but this analytical theory does not include dynamical effects (such as cloud compression) that further reduce the evaporation rate in models T1HP, T5LP and T5HP. The net effect is for an increase cloud survival times in cases where $\sigma_0 \gtrsim 0.25$ in comparison to the values predicted from Cowie & McKee (1977).

If we define a cloud lifetime as $\tau_{\text{life}} = M_{\text{cloud}}/\dot{M}_{\text{cloud}}$, and using the mean cloud mass loss rate found in the simulations, then the cloud life times in the conductive models are as follows. Model T1LP: 12.8 Myr; Model T1HP: 3.3 Myr; Model T5LP: 2.0 Myr; Model T5HP: 0.9 Myr. With the exception of model T1LP, these lifetimes are somewhat less than the lifetime we expect the average cloud in a superwind should have.

The mean mass loss rate in the simulation of the cloud with $R_c = 45$ pc is $\dot{M}_{\text{cloud}} = 6.26 \times 10^{-5} M_{\odot} \text{ yr}^{-1}$, three times larger than in the analogous model T1LP with the standard radius $R_c = 15$ pc ($1.93 \times 10^{-5} M_{\odot} \text{ yr}^{-1}$). Conduction is not saturated in this model, as $\sigma_0 = 0.043$, so that the mass loss rate is classical and scales in proportion R_c . The numerical result is consistent with the theoretical expectation. In fact, the Cowie & McKee formula (Equ. 1) yields $\dot{M}_{\text{cloud}} = 1.84 \times 10^{-5} M_{\odot} \text{ yr}^{-1}$ for $R_c = 15$ pc, and $5.52 \times 10^{-5} M_{\odot} \text{ yr}^{-1}$ for $R_c = 45$ pc (These values are obtained considering a temperature $T = 2 \times 10^6$ K measured from the simulations between the bow shock and the cloud [instead of the theoretical bow-shock temperature], and halving the values obtained considering the lower temperature at the rear of the cloud). The cloud lifetime scales as R^2 in the classical regime, as expected. Note however that if dynamical effects were important (as in all models but T1LP) we expect a lifetime longer than the theoretical one. To summarize, cloud lifetime is a strong function of cloud size. Conductive clouds larger than the default $R_c = 15$ pc we consider may well have survival times equivalent to wind flow times, even in the case of conduction at Spitzer levels.

It is difficult to assess cloud lifetimes in the non-conductive models. Cloud fragments are very rapidly accelerated and advected off the fixed numerical grid we have used in these simulations. It is hard to assess what fraction of the mass loss from the cool phase is due to this process, as opposed to transfer of mass into hotter phases, or to algorithmically determine the mass of the remnant of the original cloud. Bearing these complications in mind, we have simply totaled the mass of all cool gas (again $\log T < 4.08$) on the computational grid. For each model, comparison to the equivalent conductive model at the same time shows that for all cases there is more cool gas in the non-conductive models by a factor of typically $\lesssim 15\%$ in the low wind temperature models (T1 models), and ~ 50 to 100% in the high wind temperature models (T5 models). Note that accounting for cloud fragments lost from the grid would increase these differences. In this crude sense mass loss (to the hot phase) is less in the non-conductive models. The higher total cool gas mass in the NC models is spread over multiple cloud fragments.

For model T5LPNC we did identify the cloud core by hand at $t = 1$ Myr and obtained a cold gas mass for this core of $47 M_{\odot}$. At this time the cold gas mass in conductive model T5LP is $\sim 100 M_{\odot}$. Thus in terms of maximizing the lifetime of the original cloud non-conductive models are not better than the conductive models.

The simulations we have presented should be considered to as two extremes in which cloud lifetimes are minimized: clouds experiencing conduction-driven evaporation due to conduction at effectively saturated levels, verses efficient hydrodynamical fragmentation under conditions of no conduction at all. Our brief investigation of models with

Table 6. Observed *FUSE* OVI to soft X-ray flux ratios in superwinds and normal spiral halos.

Galaxy and region	Width pc	f_{OVI} $\text{erg s}^{-1} \text{cm}^{-2}$	$f_{X,0.3-2.0}$ $\text{erg s}^{-1} \text{cm}^{-2}$	$\log L_X$	f_{OVI}/f_X	OVI ref.	X-ray ref.
(1)	(2)	(3)	(4)	(5)	(6)	(7)	(8)
M82-A	525	$< 11.4 \times 10^{-14}$	$(94.6 \pm 2.2) \times 10^{-14}$	39.2	< 0.12	1	1
M82-B	525	$< 11.4 \times 10^{-14}$	$(69.5 \pm 2.1) \times 10^{-14}$	39.0	< 0.16	1	1
M82-C	525	$< 9.3 \times 10^{-14}$	$(11.9 \pm 0.8) \times 10^{-14}$	38.3	< 0.78	1	1
M82-D	525	$< 9.5 \times 10^{-14}$	$(6.3 \pm 0.5) \times 10^{-14}$	38.0	< 1.51	1	1
NGC 3079	2490	$< 1.5 \times 10^{-14}$	$(30.7 \pm 2.9) \times 10^{-14}$	40.0	< 0.05	2	2
NGC 4631-A	1092	$(3.6 \pm 0.8) \times 10^{-15}$	$(3.6 \pm 0.9) \times 10^{-15}$	37.4	1.00 ± 0.33	3	4
NGC 4631-B	1092	$(6.2 \pm 1.0) \times 10^{-15}$	$(10.0 \pm 1.2) \times 10^{-15}$	37.8	0.62 ± 0.12	3	4
NGC 891-2	1395	$(2.1 \pm 1.1) \times 10^{-15}$	$(7.8 \pm 3.8) \times 10^{-15}$	37.9	0.27 ± 0.19	3	4

A compilation of observed *FUSE* OVI flux measurements in the halos of nearby starburst and normal spiral galaxies, along with *Chandra* ACIS-S measurements of the diffuse soft X-ray luminosity within the same region. The physical size corresponding the $30''$ angular width of the square *FUSE* LWRS aperture is given in column 2, assuming distances of 3.6, 17.1, 7.5 and 9.6 Mpc to M82, NGC 3079, NGC 4631 and NGC 891 respectively. The OVI fluxes quoted in column 3 refer to the sum of the 1032 and 1038 Å lines, assuming the flux in the 1038 Å line is exactly half that of the 1032 Å fluxes measured (the reference for which is given in column 7). The diffuse soft X-ray ($E = 0.3 - 2.0$ keV) fluxes are based on *Chandra* ACIS-S measurements, the reference for which is given in column 8. The log of the absorption-corrected soft X-ray luminosity (in units of erg s^{-1}) within the *FUSE* observation region is given in column 5. Upper limits are 3σ . Errors in fluxes, where given, are purely the statistical uncertainties in the number of OVI 1032 Å or diffuse $E = 0.3 - 2.0$ keV X-ray photons within the region encompassed by the *FUSE* aperture. All fluxes are corrected for extinction/absorption, using the Galactic extinction law (Cardelli et al. 1989) for OVI and the Morrison & McCammon (1983) model for X-ray absorption cross sections. Only Galactic foreground extinction is assumed for NGC 4631 and NGC 891, while intrinsic absorption within the wind is required for M82 (Hoopes et al. 2003) and NGC 3079 (Hoopes et al, in preparation).

References: (1) Hoopes et al. (2003). The X-ray fluxes are based on spectral fits to the diffuse X-ray emission within each of the regions covered by the *FUSE* apertures. (2) From Hoopes et al (in preparation). (3) Otte et al. (2003), (4) This work. X-ray fluxes are based on scaling the measured halo-region diffuse soft X-ray fluxes from Strickland et al. (2004) by the ratio of the $E = 0.3 - 2.0$ keV diffuse count rate in the region of the *FUSE* aperture to the total halo diffuse count rate.

conduction at sub-Spitzer levels shows that in certain circumstances conduction is strong enough to suppress the hydrodynamical instabilities that fragment clouds, while also reducing cloud evaporation. As previously discussed larger clouds also have longer lifetimes. Thus it seems plausible that it will be possible to find conditions in which simulated cloud lifetimes are the $\gtrsim 10$ Myr timescales we expected from observations, but further simulations will be required to test this hypothesis.

4.2 Conduction-driven cloud implosion and star formation

The possible role of interstellar or inter-galactic shock waves in promoting star formation (or even galaxy formation) by crushing ambient gas clouds has been considered many times (e.g. see Woodward 1976; Ostriker & Cowie 1981; Shchekinov 1989; Begelman & Cioffi 1989; Bicknell et al. 2000; Gorti & Hollenbach 2002; Fragile et al. 2004; Scannapieco et al. 2004). Nevertheless, it has long been known that shock-crushing does have some undesirable effects, as the compression is not isotropic but tends to pancake the cloud (Woodward 1976).

The conduction-driven cloud compression seen in our simulations, and first noted by Ferrara & Shchekinov (1993), should also be active in many of the contexts in which shock-driven cloud-crushing is considered, as long as hot gas is generated and thermal conduction is not completely suppressed. This conduction-driven compression is much more isotropic (due to the rapidity with which hot gas

can wrap around a cloud) than shock crushing, and achieves high compression ratios.

The clouds we have simulated are not natural candidates for star formation, given their low initial densities and masses. Nevertheless, conduction-driven implosion is a very interesting mechanism than deserves further investigation, and should be considered when thinking of extra-planar star formation in actively star-forming galaxies, and in galaxies over run by superwinds or jets.

4.3 The origin and metallicity of the X-ray emitting gas

What implications do these simulations have for understanding soft X-ray emission in superwinds? As discussed in Section 1, from observations it is clear that the majority of the soft X-ray emitting gas comes from a relatively small fraction of the total volume occupied by the wind. Current X-ray observational studies (see Strickland et al. 2004, and references therein) are consistent with the following scenarios: that the hot gas is ambient gas heated by the wind to X-ray-emitting temperatures, or alternatively is denser-than-average regions of initially hot merged SN and stellar wind ejecta, or is some mixture of the two. This is an important issue, for in hydrodynamical models of superwinds it is the merged SN ejecta that contains the majority of the energy of the wind (Strickland & Stevens 2000), and is the material most likely to escape into the IGM. If a significant fraction of the soft X-ray emission in superwinds comes from this material then future, higher-spectral resolution X-ray observatories, such as *Astro-E2* and *Constellation-X* (which

can measure the velocity of the hot gas) will be able to directly constrain metal and energy ejection from starbursts into the IGM. If the hot gas is predominantly ambient ISM then these observatories will only probe a smaller fraction of the metal flow associated with superwinds.

Observationally, the simplest diagnostic of the origin of the X-ray emitting gas would be to measure the absolute metal abundance. This has proved to be difficult, given a variety of systematic biases in the low to moderate resolution spectroscopy available with *ROSAT*, *ASCA*, *Chandra* and *XMM-Newton*. These include the artificial blending of spectrally distinct regions (Dahlem et al. 1998; Weaver et al. 2000; Dahlem et al. 2000), calibration uncertainties and over-simplistic spectral model fits to intrinsically complex spectra (Strickland & Stevens 1998). The unphysically-low X-ray derived abundances found in the earliest Chandra observations of superwinds (see e.g. Wang et al. 2001; Strickland et al. 2002; Xia et al. 2002) are almost certainly primarily due to small inaccuracies ($\lesssim 2\%$) in the ACIS energy scale available at that time. Re-analysis of that data with more modern calibrations leads to significantly larger best fit abundances that are statistically inconsistent with the previous results, although it is still effectively impossible to distinguish between Solar or super-Solar element abundances with respect to hydrogen (e.g. Martin et al. 2002; Strickland et al. 2004). In the near future observations with the much higher spectral resolution provided by the *Astro-E2* calorimeter will not suffer from these problems, and so should provide strong constraints on the absolute elemental abundances in the nearest bright superwinds.

We discussed the origin of the soft X-ray emission in our models of a wind/cloud interaction in Section 3.4. Here we restate those claims and develop our analysis further, by also considering cases where $Z_w > Z_c$.

Soft X-ray emission in the cloud models without thermal conduction (the NC models) generally arises in wind material within the bow shock (see Fig. 8), with a model-dependent contribution from the cloud surfaces. In the models with conduction the soft X-ray luminosities are typically larger (by a factor between 2 and 30) than in the non-conductive models (Table 3), and this increased luminosity is due to the increase in the hot gas density in the region between the cloud surface and the bow shock due to evaporated cloud material (see Fig. 10).

Note that the OVI luminosities of both classes of model are very similar. In these models the gas emitting OVI typically has a density of $n \sim 5 \times 10^{-2} \text{ cm}^{-3}$, and is always material originally from the cloud in both conductive and non-conductive models. As such it will have the metallicity of the unenriched cloud, i.e. low abundances if the cloud is a halo or high velocity clouds over-run by the wind, or the metallicity of the WIM of the host galaxy if it is being advected out of the disk within the wind.

The results presented in Section 3.4 were made under the assumption that the metal abundance of the wind and cloud material were both Solar. As discussed in Section 2, the metal abundance of the wind material can be considerably higher than Solar, depending on the degree of wind mass-loading. In a situation where $Z_w > Z_\odot$ wind material will make up a larger fraction of the X-ray emission, as the soft X-ray emissivity scales roughly in proportion to the metal abundance for gas in the temperature range $T \sim 10^6$

-10^7 K. Note that there must be little or no mass loading of the wind for its metal abundance to be high. Consequently the wind velocity and temperature will be higher and wind density lower than in a heavily mass-loaded case. Thus our T1 models could be considered as representing heavily mass loaded winds, and the T5 models as non-mass loaded or weakly mass loaded winds.

To illustrate the influence of the wind metal abundance on the emission from the wind/cloud interaction, we recomputed the X-ray luminosity as function of time in all models assuming that the X-ray emissivity of all wind material was either 4 or 10 times higher than for a Solar abundance plasma. In Fig. 12 we show the ratio of this luminosity $L_X(Z)$ to the X-ray luminosities calculated assuming $Z_w = Z_\odot$ (which were shown in Fig. 9) as a function of time. Changing the abundance of the wind material will have negligible effect on the OVI emission, which is always dominated by cloud material.

The large increase in X-ray luminosity seen in the T5LPNC models for high Z_w illustrates the dominance of wind material in this model (long dashed lines in Fig. 12a and b). Averaged over the entire length of the simulations wind fluid material accounts for 35% of the soft X-ray emission when $Z_w = 1Z_\odot$. This fraction increases to 88% (95%) if $Z_w = 4Z_\odot$ ($Z_w = 10Z_\odot$). In contrast, with conduction active the wind material only accounts for on average 25% of the X-ray emission in model T5LP when $Z_w = 1Z_\odot$. Although the increase in X-ray luminosity for this model at high Z_w (see Fig. 12c and d) is significantly less than in model T5LPNC, wind material does dominate the emission (58% of the emission for $Z_w = 4Z_\odot$, 77% of the emission for $Z_w = 10Z_\odot$).

All the T1 models are on average dominated by wind material, for all values of Z_w , so the X-ray luminosity does increase strongly with increased Z_w .

The T5HP models are another interesting case. Despite the very different dynamical state of the T5HPNC and T5HP models, the average fraction of the X-ray emission from wind material in both models is relatively similar (although always slightly larger in the non-conductive NC models, representing the lack of any contribution due to strong evaporative loading of the bow shock region that is seen in the conductive model). For $Z_w = 1Z_\odot$ wind material only produces 12% of the emission in the T5HP model, and 14% of the emission in the T5HPNC. As argued previously a wind with conditions similar to those in the T5HP(NC) models can not be heavily mass-loaded, and hence will have a high metal abundance. Cloud material dominates in both of these models for $Z_w = 4Z_\odot$, but for $Z_w = 10Z_\odot$ wind material provides 57% of the emission in the T5HP model and 66% of the emission in model T5HPNC.

Our discussion using broad energy band weighted luminosities and \mathcal{R} ratios is intended primarily as an aid to understanding, but some of the subtleties and second order effects are also worth considering. Not only does the relative degree of enrichment of the wind (or Z_{SN}/Z_{ISM}) vary from element to element, but the degree of contribution of wind material (\mathcal{R}) to the X-ray emission is also element dependent, given the different temperature of the conductive interface compared to the bow shock. The emissivity of different elements and their ions are strongly temperature dependent. In these simulations the conductive inter-

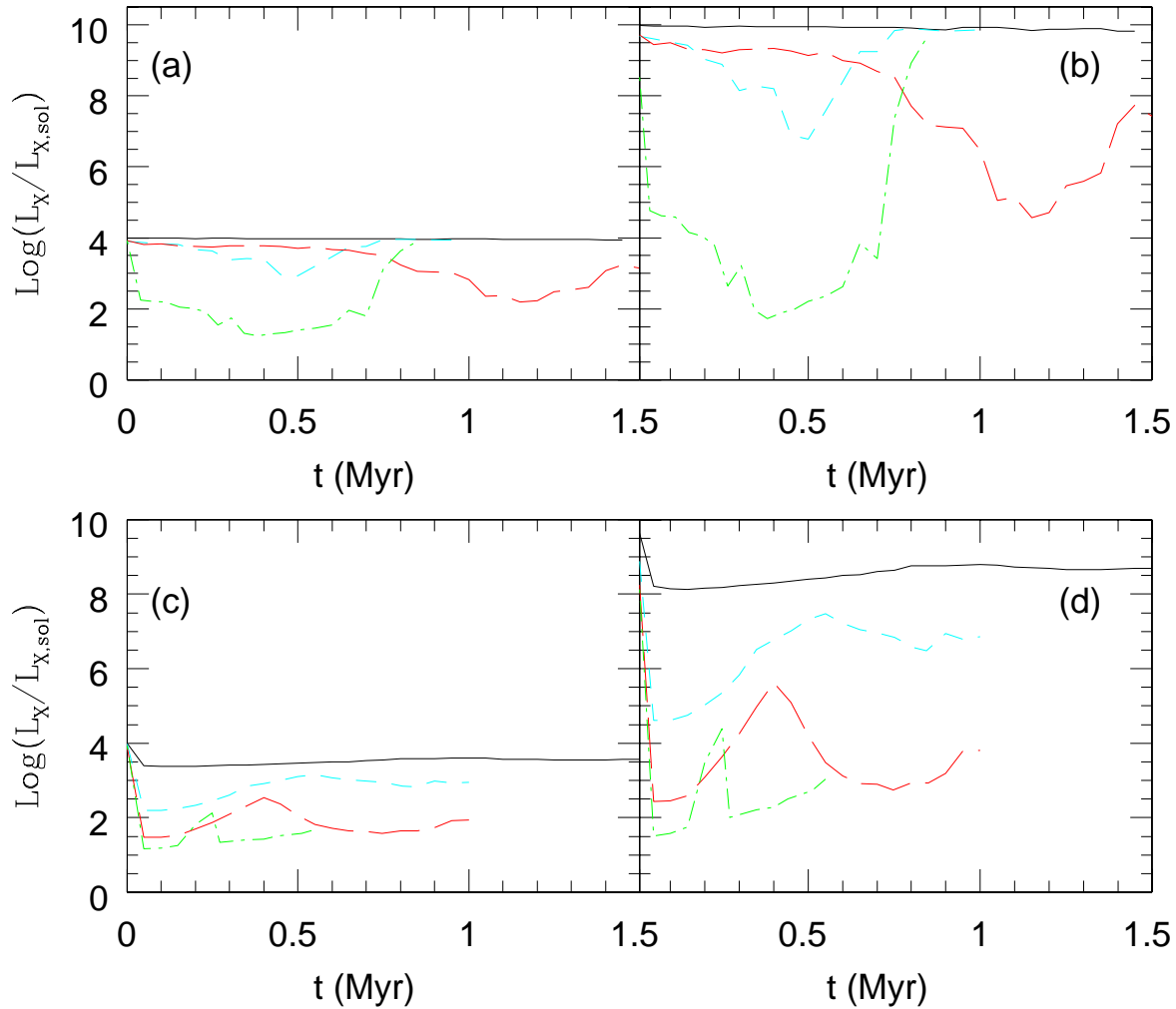


Figure 12. X-ray luminosities for high Z_w normalized to L_X obtained with $Z_w = 1Z_\odot$. Black solid lines: T1LP(NC); blue short dashed: T1HP(NC); red long dashed: T5LP(NC); green dot dashed: T5HP(NC). In all cases $Z_c = 1Z_\odot$. (a) Non-conductive models, assuming $Z_w = 4Z_\odot$. (b) Non-conductive models, assuming $Z_w = 10Z_\odot$. (c) Conductive models, assuming $Z_w = 4Z_\odot$. (d) Conductive models, assuming $Z_w = 10Z_\odot$.

face has a lower temperature than the wind bow shock, and thus emission from lower-temperature ions (e.g. OVII or OVIII) will be more heavily influenced by cloud material than higher temperature ions (e.g. MgXI, MgXII or SiXIII). In some cases, particularly when conductive-interface and wind contributions are on average comparable, this effect would lead to peculiar X-ray-derived abundance patterns, with lower ionization state ions appearing to have lower abundances than high-ionization ions. It is conceivable that the peculiarly-low X-ray-derived ratio of Oxygen to other α -element abundances found in M82 by Origlia et al. (2004) might be caused by such an effect, although there are a few other observational biases that could also cause these odd results.

The point that should be taken away is the gas probed by soft X-ray observations of superwinds is not necessarily always un-enriched ambient gas even when thermal conduction is active at the high Spitzer-conductivity levels. For

some sets of conditions (and counter to naïve expectation), in particular in powerful high velocity and high pressure winds, the ambient gas being conductively evaporated off the cloud does dominate the observable soft X-ray emission. In less powerful winds conductive evaporation is reduced, and in these case and in the case of no conduction, the soft X-ray emission arises in wind material within the bow shock around each cloud. The metal abundance of the wind material depends strongly on the degree of mass-loading of the volume-filling wind-fluid, which is a separate topic deserving some additional investigation. However, this implies that if we can measure the metal abundance of the soft X-ray emitting gas it can be representative of the more tenuous volume-filling wind, and thus can be used to constrain the degree of large-scale wind mass loading.

4.4 Soft X-ray and OVI emission and absorption

4.4.1 OVI absorption

The mean OVI column densities through a simulated single wind/cloud interaction (Table 4) are typically 1.5 dex lower than the value of N_{OVI} seen in starbursts observed with *FUSE*, which range from $14.3 < \log N_{\text{OVI}} < 15.3$ (see Heckman et al. 2002). Increasing the cloud radius, or the metal abundance of the wind, is not likely to increase N_{OVI} , for the reasons discussed in Section 3.6 and Section 4.3.

There is relatively little difference in mean N_{OVI} between the conductive and non-conductive models. While it is hard to assess to what degree numerical diffusion is artificially increasing the amount of OVI absorbing material in the non-conductive models, it is certainly true that N_{OVI} is not currently a strong discriminant between conductive and non-conductive models for wind/cloud interactions.

The hotter and/or faster wind models produce larger mean N_{OVI} per cloud. A high mean N_{OVI} per cloud is advantageous, in that it reduces the number of clouds needed to match observations. Unfortunately, cloud stripping or evaporation is more efficient in such models, so either more clouds would be required initially, or a continuous source of clouds would be required (e.g. via Kelvin-Helmholtz instabilities along the walls of the cavity).

There would need to be ~ 30 clouds per line of sight if clouds alone are responsible for the OVI absorption in superwinds. In practice the walls of the outflow will be another significant source of OVI absorption. That there should be multiple clouds along any line of sight through a superwind is by no means surprising, given that the velocity width of observed optical and UV absorption lines is much greater than could be expected from any single structure. Nevertheless, a model requiring very large numbers of clouds along any line of sight is neither parsimonious nor elegant. In summary, the simulated OVI column densities alone do not provide strong constraints on allowable wind models when compared to the existing observations.

As shown in Heckman et al. (2002) superwinds follow a distinct OVI column density vs line width (b) relationship. We would expect that the column density and line width of a simulated OVI profile from a single cloud should fall on the trends shown in Fig. 1 of that paper if a superposition of clouds is to create the net profile observed. Of the simulated OVI profiles we investigated only half of them fell on the low N_{OVI} , low b extrapolation of the Heckman et al. (2002) trend. The other simulated profiles had low N_{OVI} but high b values of ~ 200 km/s. This is puzzling, but it is too early to assess if this is a significant discrepancy. Our simulations only cover the first 1 Myr of a cloud/wind interaction, while real superwinds should contain clouds with a broad range of ages.

4.4.2 OVI and soft X-ray emission

In Table 6 we summarize the published values of OVI and soft X-ray fluxes in three starburst-driven superwinds (M82 and NGC 3079 host strong superwinds, while NGC 4631 is a weaker starburst) and the marginal OVI detection in the halo of a normal spiral galaxy believed to have a galactic fountain (NGC 891), adapted from the work of Hoopes et al. (2003)

and Otte et al. (2003). We choose to concentrate our analysis on the ratio of OVI to soft X-ray emission, and the ratio of the emitted FUV and X-ray power to the wind mechanical power, given that we can only simulate a single cloud. The $30''$ -wide aperture of the *FUSE* observations samples a small fraction of the total region covered by soft X-ray emission in these objects, but this is considerably larger than volume we can simulate with high resolution.

Note even with the limited observational data currently available it is clear that there is not a single universal $L_{\text{OVI}}/L_{\text{X}}$ ratio in superwinds: the upper limits on the ratio in M82 and N3079 are significantly lower than the values based on a statistically strong detection of OVI in the NGC 4631 wind.

The value of the wind mechanical luminosity intercepted by the cloud, used in Table 3, is calculated over a radius of 10 pc, which is roughly the mean radius the compressed or crushed clouds assume. Note that the X-ray and OVI luminosities are calculated using a larger radius of 50 pc (in order to encompass the majority of the bow shock around the cloud). This mismatch in radii is reasonable, as the X-ray emission region is always larger than the cloud itself. If we were to use a 50 pc radius for both L_{mec} and the emitted radiation then the mean $L_{\text{OVI}}/L_{\text{mec}}$ and $L_{\text{X}}/L_{\text{mec}}$ ratios would be lower by a factor 25.

By using a radius equivalent to the effective cloud radius in calculating L_{mec} , and hence the $L_{\text{OVI}}/L_{\text{mec}}$, $L_{\text{X}}/L_{\text{mec}}$ and $L_{\text{tot}}/L_{\text{mec}}$ ratios, we are effectively assuming the cloud area covering factor (as seen by the wind) is of order unity. If the cloud covering factor is less than unity, then the mean radiative to mechanical energy ratios should be reduced proportionally. However, it should be noted that FUV spectra of starbursts taken with *FUSE* indicate that the area covering fraction of neutral atomic clouds (e.g. seen in CII $\lambda 1036$ absorption) is indeed of order unity (Heckman et al. 2001a), in contrast to the lower area covering fraction of (presumably denser) molecular gas clouds (Hoopes et al. 2004).

Table 3 shows the mean fraction of wind mechanical energy converted in X-ray or FUV radiation *by a single cloud* of initial radius 15 pc, along with the mean OVI to soft X-ray flux ratio. As OVI emission accounts for $\sim 30\%$ of the total emissivity of gas at $T \approx 3 \times 10^5$ K, we can combine the OVI luminosities with the soft X-ray luminosities to gain an estimate of total radiative energy loss from the coronal and hot phases.

We find that a low fraction of the wind mechanical energy intercepted by a single cloud is lost to radiation. The total fraction of wind energy radiated per cloud found in the models assuming $Z_{\text{w}} = 1Z_{\odot}$ lies in the range $\sim 0.25 - 1\%$, and is relatively similar between the conductive and non-conductive models. For higher values of Z_{w} the ratio $L_{\text{X}}/L_{\text{mec}}$ per cloud is still $\lesssim 1\%$, except in the T1LP and T1LPNC models where it reaches $2 - 3\%$. As mentioned previously a somewhat larger fraction of wind energy ends up as cloud kinetic energy.

The simulations show that a superwind can flow around a cloud and thus affect multiple clouds along any particular path without any substantial radiative loss of wind energy, except in the case of the T1LP(NC) models where radiative losses may violate observational limits. Summed over all clouds the $L_{\text{tot}}/L_{\text{mec}}$ ratio should not significantly exceed estimates of the X-ray and FUV luminosity to wind

mechanical power in real superwinds. Using *FUSE* observations of the dwarf starburst NGC 1705, Heckman et al. (2001b) limit to the coronal cooling rate to be $\sim 5/\epsilon\%$ of the mechanical luminosity based on the observed OVI absorption line strength. Soft X-ray observations of superwinds give a ratio of $\sim 1/\epsilon - 3/\epsilon\%$ for the X-ray to mechanical power ratio (Strickland 2004). The major uncertainty in these observationally-derived ratios is the unknown efficiency of supernovae energy thermalization ϵ .

The lower pressure wind models (LP models) produce more emission per unit mechanical power than the high pressure models, although the magnitude of L_{OVI} or L_{X} is larger per cloud in the high pressure models. The lower temperature wind models (all T1 models) also produce more emission per unit L_{mec} than the higher temperature wind models, but this is mainly because of the high wind density in these models.

In accord with the observational evidence, coronal phase cooling (i.e. emission predominantly in the FUV) dominates over X-ray cooling from hotter gas by a factor of at least a few. The strongest difference between the models consists in the X-ray cooling efficiencies. With the one exception of model T1LPNC, the $L_{\text{X}}/L_{\text{mec}}$ ratios are an order of magnitude lower in non-conductive models compared to the models with conduction.

Another significant difference between the conductive and non-conductive clouds models is in the OVI to X-ray luminosity ratio. In our opinion this ratio places the most interesting constraints on whether wind/cloud interaction models can reproduce observed superwind properties.

For $Z_{\text{w}} = Z_{\odot}$ the majority of the non-conductive models have $L_{\text{OVI}}/L_{\text{X}}$ ratios that are orders of magnitude larger than the largest values observed to date (compare Table 3 to Table 6). The low pressure non-conductive model T1LPNC has $L_{\text{OVI}}/L_{\text{X}} = 1.07$, but this value is still much larger than the upper limits on the $L_{\text{OVI}}/L_{\text{X}}$ ratio for M82 and NGC 3079.

The conductive models span a much smaller range in $L_{\text{OVI}}/L_{\text{X}}$, from 0.2 to 2.7. Again, the low temperature low ram pressure models have the lowest $L_{\text{OVI}}/L_{\text{X}}$ ratios, closer to the observed range, if still only matching the values observed in NGC 4631.

The fundamental problem with the non-conductive models are the low X-ray luminosities. The OVI luminosities are comparable in both conductive and non-conductive models, so it is the higher soft X-ray luminosities generated by cloud material in the conductive interface that leads to roughly acceptable $L_{\text{OVI}}/L_{\text{X}}$ ratios. It may be the case that the typical $L_{\text{OVI}}/L_{\text{X}}$ ratio in superwinds is $\lesssim 0.1$, in which all of our wind/cloud interaction models have trouble producing a realistic $L_{\text{OVI}}/L_{\text{X}}$ ratio if $Z_{\text{w}} \sim Z_{\text{c}}$.

Larger clouds are more effective at intercepting wind energy and converting it into radiation. The mechanical power intercepted scales as R_{c}^2 , but the X-ray emission scales as roughly R_{c}^3 over the small range of radii we have investigated (see Section 3.6). The OVI luminosity does not grow with increased radius as rapidly as the X-ray luminosity, so the $L_{\text{OVI}}/L_{\text{X}}$ ratio per cloud will drop as for clouds of larger radius. This effect is probably not significant enough to reconcile the low Z_{w} non-conductive models with observed $L_{\text{OVI}}/L_{\text{X}}$ ratios, but should be considered for the conductive models. In the case of models with thermal con-

duction, matching the $L_{\text{OVI}}/L_{\text{X}}$ ratio in M82 and NGC 3079 is possible if the average cloud has an initial radius only a few times larger than 15 pc. Larger cloud radii also have the added advantage of longer cloud lifetimes, as previously discussed.

Even values of $Z_{\text{w}} = 10Z_{\odot}$ are not sufficient to produce acceptably low $L_{\text{OVI}}/L_{\text{X}}$ for the non-conductive models (see Table 3). However, for the conductive models a high Z_{w} value does produce $L_{\text{OVI}}/L_{\text{X}}$ values similar to the $L_{\text{OVI}}/L_{\text{X}} \lesssim 0.1$ upper limit in M82 and NGC 3079. Thus even in the case of $Z_{\text{w}} \gg Z_{\text{c}}$ the OVI to X-ray ratio appears to provide a strong discriminant between non-conductive and conductive cloud models for superwinds, with conductive models producing values in the range of those observed.

Furthermore, it appears that we need not require conduction at full Spitzer levels to attain acceptably low $L_{\text{OVI}}/L_{\text{X}}$ ratios. As shown in Table 5 a reduction in the value of the coefficient of thermal conductivity by a factor $f = 5$ barely altered the time-averaged $L_{\text{OVI}}/L_{\text{X}}$ ratio. Even for a reduction of $f = 25$ the increase in $L_{\text{OVI}}/L_{\text{X}}$ is surprisingly small. Conduction is still dynamically important in these models in stabilizing the cloud against fragmentation, so it is possible that with weak to moderate conduction we can produce longer-lived clouds with suitably low $L_{\text{OVI}}/L_{\text{X}}$ ratios. Further simulations tracking clouds over significantly longer timescale will be necessary to test this hypothesis.

For the set of parameters investigated in this paper the models T1HP and T5LP have the most acceptable X-ray and OVI emission properties, in that the $L_{\text{tot}}/L_{\text{mec}}$ ratio per cloud is not too large (even in cases where $Z_{\text{w}} \sim 10Z_{\odot}$) and the $L_{\text{OVI}}/L_{\text{X}}$ ratio is also low.

5 SUMMARY

We performed a series of 2-dimensional hydrodynamical simulations with a resolution 0.1 pc of a super-or-Hyper-sonic starburst-driven superwind interacting with an initially stationary cool dense cloud of radius $R_{\text{c}} = 15$ pc. Such interactions are one of a class of wind/cloud interactions known to occur within superwinds. Wind/cloud interactions may play a significant role in shaping their observable properties, in particular in the FUV and X-ray energy bands, but have not been explored numerically in any detail. More general analytical models often applied to superwinds, such as the Weaver et al. (1977) wind-blown bubble model, have trouble explaining observed OVI absorption line column densities and OVI to X-ray emission flux ratios.

We considered a range of models, with low and high wind ram pressure (both pressures are much higher than conventional ISM pressures), low and high wind to cloud density ratios, and the presence or absence of thermal conduction. The resolution of the simulations is high enough that the region of the conductive interface in which the strong coolant OVI is produced is numerically resolved. A numerical tracer field was used to distinguish between gas originally part of the cloud and gas from the wind. We followed the evolution of the wind/cloud interaction for times up to 1.5 Myr, at which point the cloud has been carried off the numerical grid by the wind. In addition to considering the dynamics of the wind/cloud interactions, we have also modeled their soft X-ray emission and FUV OVI emission

and absorption properties and compared them to existing observational data.

There are significant dynamical differences between wind/cloud interactions in the presence of thermal conduction compared to those without conduction. In the absence of conduction the clouds are fragmented in a few dynamical (cloud-crushing) time-scales $\tau_{cc} = \chi^{1/2} R_c / v_w$ (where $\chi = \rho_c / \rho_w$), as expected from earlier of clouds over-run by SN blast waves (Klein et al. 1994). Relatively little cool cloud mass is converted into hot gas by shocks or mixing, but the cloud rapidly ceases to exist as a recognizable coherent object due to the hydrodynamical instability-driven fragmentation.

In contrast, thermal conduction acts to stabilize the cloud by inhibiting the growth of Kelvin-Helmholtz and Rayleigh-Taylor instabilities (as had previously been found in the case sub-sonic motion of Molecular clouds in a hot medium by Vieser & Hensler 2000). Furthermore, the conductive heat flux into the cloud's surface generates a shock wave that compresses the cloud and modifies its internal density structure significantly and reduces its conductive mass loss rate (as previously discovered for stationary clouds by Ferrara & Shchekinov 1993). These dynamical effects occur even in models in which the coefficient of thermal conductivity has been reduced by factors of up to 25 from the Spitzer value. If thermal conduction is active, then clouds embedded within a superwind will exist as a single coherent structure for longer time scales than they otherwise would, *but* at the cost of losing mass to evaporative heating. The strength of these conductive effects is proportional to the dimensionless parameter σ_0 (Equation 2). This parameter is high for low density winds, small clouds, and high wind temperature, especially in the case of supersonic winds where the temperature of material in the bow shock around the cloud is greater than the wind temperature.

In general, the higher the wind ram pressure or velocity is, the higher the mass loss rate of a cloud will be, due to either hydrodynamical fragmentation or conductive evaporation.

With or without the presence of thermal conduction, OVI emitting and absorbing material primarily arises in cloud material at the periphery of the cloud and any cloud fragments. In contrast, the origin of the soft X-ray emitting material depends on the strength of conductive effects and the relative metal abundances of the wind and cloud material. If conductive effects are weak or absent, and/or the metal abundance of the wind Z_w is highly enriched compared to the cloud Z_c , then the observed soft X-ray emission comes from wind material in the bow shock around the cloud. Thus even if the undisturbed superwind is relatively tenuous and thus a weak X-ray emitter, when compressed around an obstacle such as a cloud its emission is enhanced and hence the wind abundance pattern could be probed by soft X-ray observations. For strong conduction, or in the case of weaker conduction with $Z_w \sim Z_c$ (e.g. a heavily mass-loaded superwind) the X-ray emission again arises within the bow shock region, but conductively evaporated cloud material mixed into this region dominates the emissivity. In the highest wind ram pressure and wind temperature models with conduction or without conduction it is still cloud material that dominates the X-ray emission, even

if the metal abundance of the wind is 10 times greater than that of the cloud.

Thus whether soft X-ray observations probe wind or cloud material in a wind/cloud interaction depends on several factors: primarily the strength of conduction (conduction favouring cloud material) and the relative abundances of wind with respect to the cloud (if the wind is strongly enriched then its influence increases). Different material can in principle be seen at different X-ray energies, with low ionization species such as Oxygen being more strongly weighted toward probing the cooler conductive interface than high ionization species such as Mg or Si (which would tend to probe the hotter regions of the bow shock). This complexity may contribute to some of the uncertainties and peculiarities found in current X-ray-derived metal abundances in starbursts (e.g. Origlia et al. 2004).

The OVI absorption line column density produced per cloud is relatively similar between conductive and non-conductive models, ranging from $12.9 \lesssim \log N_{\text{OVI}} \lesssim 13.5$. In all cases the mean N_{OVI} value found is substantially less than the observed total OVI column densities in starbursts with winds, so that in the wind/cloud interaction model requires many clouds per line of sight (typically 10 – 30 clouds). Models with stronger hydrodynamical stripping or conductive evaporation produce higher mean N_{OVI} , but their shorter cloud lifetimes are disadvantageous for accumulating larger numbers of clouds, and maintaining cool cloud gas populations in winds for the ~ 10 Myr time periods that appear to be implied by observations.

In terms of emission we considered two primary observational constraints. The strongest observation constrain is the ratio between OVI and soft X-ray emission L_{OVI}/L_X , which has the value ~ 1 in NGC 4631 (this work, see also Otte et al. 2003), and is definitely much lower ($\lesssim 0.1$) in the stronger M82 and NGC 3079 superwinds (Hoopes et al. 2003, Hoopes et al, in preparation). The second is that observations place limits on the fraction of wind mechanical power that is radiated in the FUV and X-ray bands, which are relatively low (e.g. $\lesssim 5/\epsilon\%$) but made somewhat uncertain by our lack of robust knowledge of the starburst SN thermalization efficiency ϵ . We found that except for the low ram pressure low wind temperature T1LP(NC) models, $\lesssim 1\%$ of the wind mechanical energy is lost to radiation per cloud, even for wind metal abundances as high as $10Z_\odot$. Typically between 2 – 6% of the wind mechanical energy ends up as kinetic energy of the cold cloud within the first 0.5 Myr.

If we consider both possible cases, of both Solar and super-Solar abundance winds, we can draw the following conclusions. Qualitatively, the high wind-ram pressure models or the low ram pressure high wind temperature model are somewhat better than the low pressure, low wind temperature, models at matching the available constraints on X-ray emission and OVI emission and absorption. If $Z_w \sim Z_c$ then the non-conductive models are ruled out by their very high L_{OVI}/L_X ratios (due to the relative lack of X-ray emission), while conductive models can match the value of ~ 1 observed in NGC 4631. Even if $Z_w = 10Z_\odot$ then the L_{OVI}/L_X ratio in most of the non-conductive models remains higher than the value observed in NGC 4631. For high Z_w the conductive models produce L_{OVI}/L_X as low as ~ 0.1 , similar to the upper limits on the ratio in M82 and NGC 3079.

Thus some, but not all, of our current wind/cloud interaction models can match the range of L_{OVI}/L_X values observed in the starbursts NGC 4631, M82 and NGC 3079, if conduction is active, and/or with high wind metallicity (i.e. little wind mass loading). The low wind ram pressure, low wind temperature models (T1LP/NC) radiate too large a fraction of the wind's mechanical energy per cloud to allow large numbers of clouds along any line of sight, which may rule them out as a plausible model. A smaller fraction of the superwind's energy is radiated per cloud in the high pressure models, but the total luminosity per cloud is slightly higher. This is advantageous, as fewer clouds are required instantaneously, but the ultimate issue of cloud lifetime and replacement still remains. Larger clouds or lower thermal conductivity are plausible ways in which cloud lifetimes can be extended to the ~ 10 Myr time scales required by observations.

Wind/cloud interactions in superwinds have been discussed qualitatively for a long time, stretching at least as far back as the seminal paper of Chevalier & Clegg (1985). The conditions that appear to favor long cloud life times are not necessarily those that appear to produce the best match to FUV and X-ray emission and absorption properties, but it does appear that these competing requirements can be balanced. More work is required to follow clouds for longer periods, and to better investigate cloud acceleration and thermal conduction at sub-Spitzer levels.

That there is some level of diversity in the physical conditions within different starburst-driven superwinds and thus in their emitted radiation is not totally unexpected. In principle this can be advantageous if we are to disentangle the multiple fluids variables that shape a superwind and understand their physics. Observing more superwinds in detail, especially with *FUSE*, will be scientifically profitable.

Nevertheless, we find it very encouraging that some of these wind/cloud models can quantitatively match some of the observed properties of winds. Furthermore, these simulations have been very enlightening with regard to the both the role conduction may play in winds (a topic that has seen very little direct work despite its obvious potential importance), and to what controls which material (cloud or wind) is probed by X-ray observations. This latter issue is apposite given the immanent launch of the very high spectral resolution X-ray micro-calorimeter on *Astro-E2*. With direct observational probes of the elemental composition and possibly the kinematics of the soft X-ray-emitting gas in superwinds it will be possible to constrain the physical processes that shape emission from these outflows.

ACKNOWLEDGMENTS

We are grateful to the referee for his/her helpful suggestions which improved the presentation of the paper. We acknowledge financial support from National Institute for Astrophysics (INAF). The simulations were run at the CINECA Supercomputing Centre with CPU time assigned thanks to INAF-CINECA grant. One of us (A.M.) thanks the Johns Hopkins University for hospitality during work on this paper.

REFERENCES

- Adelberger K. L., Steidel C. C., Shapley A. E., Pettini M., 2003, *ApJ*, 584, 45
- Aloisi A., Savaglio S., Heckman T. M., Hoopes C. G., Leitherer C., Sembach K. R., 2003, *ApJ*, 595, 760
- Anders E., Grevesse N., 1989, *Geochim. Cosmochim. Acta*, 53, 197
- Asai N., Fukuda N., Matsumoto R., 2004, *ApJ*, 606, L105
- Axon D. J., Taylor K., 1978, *Nature*, 274, 37
- Bedogni R., D'Ercole A., 1986, *A&A*, 157, 101
- Begelman M. C., Cioffi D. F., 1989, *ApJ*, 345, L21
- Bicknell G. V., Sutherland R. S., van Breugel W. J. M., Dopita M. A., Dey A., Miley G. K., 2000, *ApJ*, 540, 678
- Bland J., Tully B., 1988, *Nature*, 334, 43
- Bland-Hawthorn J., 1995, *PASA*, 12, 190
- Cardelli J. A., Clayton G. C., Mathis J. S., 1989, *ApJ*, 345, 245
- Castor J., McCray R., Weaver R., 1975, *ApJ*, 200, L107
- Cecil G., Bland-Hawthorn J., Veilleux S., 2002, *ApJ*, 576, 745
- Cecil G., Bland-Hawthorn J., Veilleux S., Filippenko A. V., 2001, *ApJ*, 555, 338
- Chandran B. D. G., Maron J. L., 2004, *ApJ*, 602, 170
- Chevalier R. A., Clegg A. W., 1985, *Nature*, 317, 44
- Cowie L. L., McKee C. F., 1977, *ApJ*, 211, 135
- Cowie L. L., McKee C. F., Ostriker J. P., 1981, *ApJ*, 247, 908
- Dahlem M., 1997, *PASP*, 109, 1298
- Dahlem M., Parmar A., Oosterbroek T., Orr A., Weaver K. A., Heckman T. M., 2000, *ApJ*, 538, 555
- Dahlem M., Weaver K. A., Heckman T. M., 1998, *ApJS*, 118, 401
- D'Ercole A., Brighenti F., 1999, *MNRAS*, 309, 941
- Devine D., Bally J., 1999, *ApJ*, 510, 197
- Edgar R. J., Chevalier R. A., 1986, *ApJ*, 310, L27
- Ettori S., Fabian A. C., 2000, *MNRAS*, 317, L57
- Fabbiano G., Trinchieri G., 1984, *ApJ*, 286, 491
- Ferrara A., Shchekinov Y., 1993, *ApJ*, 417, 595
- Fragile P. C., Murray S. D., Anninos P., van Breugel W., 2004, *ApJ*, 604, 74
- Frye B., Broadhurst T., Benítez N., 2002, *ApJ*, 568, 558
- González Delgado R. M., Leitherer C., Heckman T., Lowenthal J. D., Ferguson H. C., Robert C., 1998, *ApJ*, 495, 698
- Gorti U., Hollenbach D., 2002, *ApJ*, 573, 215
- Heckman T. M., 1998, in *ASP Conf. Ser. 148, Origins*, Woodward C. E., Shull J. M., Thronson H. A., eds., ASP, San Francisco, p. 127
- , 2005, in *Astrophysics in the Far Ultraviolet: Five Years of Discovery with FUSE*, Sonneborn G., Moos W., Andersson B.-G., eds., *PASP*
- Heckman T. M., Armus L., Miley G. K., 1987, *AJ*, 93, 276
- , 1990, *ApJS*, 74, 833
- Heckman T. M., Lehnert M. D., Strickland D. K., Armus L., 2000, *ApJS*, 129, 493
- Heckman T. M., Norman C. A., Strickland D. K., Sembach K. R., 2002, *ApJ*, 577, 691
- Heckman T. M., Sembach K. R., Meurer G. R., Leitherer C., Calzetti D., Martin C. L., 2001a, *ApJ*, 558, 56
- Heckman T. M., Sembach K. R., Meurer G. R., Strickland D. K., Martin C. L., Calzetti D., Leitherer C., 2001b, *ApJ*, 554, 1021

- Hoopes C. G., Heckman T. M., Strickland D. K., Howk J. C., 2003, *ApJ*, 596, L175
- Hoopes C. G., Sembach K. R., Heckman T. M., Meurer G. R., Aloisi A., Calzetti D., Leitherer C., Martin C. L., 2004, *ApJ*, 612, 825
- Indebetouw R., Shull J. M., 2004, *ApJ*, 605, 205
- Kaastra J. S., Mewe R., 1993, *Legacy*, 3, 16
- Klein R. I., McKee C. F., Colella P., 1994, *ApJ*, 420, 213
- Kunth D., Mas-Hesse J. M., Terlevich E., Terlevich R., Lequeux J., Fall S. M., 1998, *A&A*, 334, 11
- Lamb H., 1945, *Hydrodynamics*. Dover, New York
- Landau L. D., Lifshitz E. M., 1987, *Course of Theoretical Physics, Vol. 6: Fluid Mechanics*, 2nd Ed. Pergamon Press
- Lehnert M. D., Heckman T. M., 1995, *ApJS*, 97, 89
- , 1996, *ApJ*, 462, 651
- Lehnert M. D., Heckman T. M., Weaver K. A., 1999, *ApJ*, 523, 575
- Leitherer C., et al., 1999, *ApJS*, 123, 3
- Liedahl D. A., Osterheld A. L., Goldstein W. H., 1995, *ApJ*, 438, L115
- Mac Low M., McCray R., 1988, *ApJ*, 324, 776
- Martin C. L., Kobulnicky H. A., Heckman T. M., 2002, *ApJ*, 574, 663
- Mathews W. G., Bregman J. N., 1978, *ApJ*, 224, 308
- McCarthy P. J., Heckman T., van Breugel W., 1987, *AJ*, 93, 264
- McKee C. F., Cowie L. L., 1975, *ApJ*, 195, 715
- , 1977, *ApJ*, 215, 213
- Mellema G., Kurk J. D., Röttgering H. J. A., 2002, *A&A*, 395, L13
- Mewe R., Gronenschild E. H. B. M., van den Oord G. H. J., 1985, *A&AS*, 62, 197
- Mewe R., Kaastra J. S., Liedahl D. A., 1995, *Legacy*, 6, 16
- Morrison R., McCammon D., 1983, *ApJ*, 270, 119
- Narayan R., Medvedev M. V., 2001, *ApJ*, 562, L129
- Norman M. L., Wilson J. R., Barton R. T., 1980, *ApJ*, 239, 968
- Ohyama Y., et al., 2002, *PASJ*, 54, 891
- Origlia L., Ranalli P., Comastri A., Maiolino R., 2004, *ApJ*, 606, 862
- Ostriker J. P., Cowie L. L., 1981, *ApJ*, 243, L127
- Otte B., Murphy E. M., Howk J. C., Wang Q. D., Oegerle W. R., Sembach K. R., 2003, *ApJ*, 591, 821
- Pettini M., Shapley A. E., Steidel C. C., Cuby J., Dickinson M., Moorwood A. F. M., Adelberger K. L., Giavalisco M., 2001, *ApJ*, 554, 981
- Pettini M., Steidel C. C., Adelberger K. L., Dickinson M., Giavalisco M., 2000, *ApJ*, 528, 96
- Phillips A. C., 1993, *AJ*, 105, 486
- Raymond J. C., Smith B. W., 1977, *ApJS*, 35, 419
- Read A. M., Ponman T. J., Strickland D. K., 1997, *MNRAS*, 286, 626
- Ritchmyer R. D., Morton K. W., 1967, *Difference methods for initial-value problems*, 2nd Ed. Interscience, New York
- Scannapieco E., Weisheit J., Harlow F., 2004, *ApJ*, 615, 29
- Schurch N. J., Roberts T. P., Warwick R. S., 2002, *MNRAS*, 335, 241
- Shchekinov I. A., 1989, *Ap&SS*, 152, 43
- Shu F., 1992, *The physics of astrophysics, Vol. II: Gas Dynamics*. University Science Books
- Strickland D., 2002, in *ASP Conf. Ser. 253: Chemical Enrichment of Intracluster and Intergalactic Medium*, Fusco-Femiano R., Matteucci F., eds., ASP, San Francisco, p. 387
- , 2004, in *IAU 222: The interplay among Black Holes, Stars and ISM in Galactic Nuclei*, Bergmann T. S., Ho L., Schmitt H., eds., CUP, Cambridge, pp. 249–254
- Strickland D. K., Heckman T. M., Colbert E. J. M., Hoopes C. G., Weaver K. A., 2004, *ApJS*, 151, 193
- Strickland D. K., Heckman T. M., Weaver K. A., Dahlem M., 2000, *AJ*, 120, 2965
- Strickland D. K., Heckman T. M., Weaver K. A., Hoopes C. G., Dahlem M., 2002, *ApJ*, 568, 689
- Strickland D. K., Stevens I. R., 1998, *MNRAS*, 297, 747
- , 2000, *MNRAS*, 314, 511
- Suchkov A. A., Balsara D. S., Heckman T. M., Leitherer C., 1994, *ApJ*, 430, 511
- Suchkov A. A., Berman V. G., Heckman T. M., Balsara D. S., 1996, *ApJ*, 463, 528
- Sutherland R. S., Dopita M. A., 1993, *ApJS*, 88, 253
- Vieser W., Hensler G., 2000, *Ap&SS*, 272, 189
- Vikhlinin A., Markevitch M., Forman W., Jones C., 2001, *ApJ*, 555, L87
- Wang Q. D., Immler S., Walterbos R., Lauroesch J. T., Breitschwerdt D., 2001, *ApJ*, 555, L99
- Watson M. G., Stanger V., Griffiths R. E., 1984, *ApJ*, 286, 144
- Weaver K. A., Heckman T. M., Dahlem M., 2000, *ApJ*, 534, 684
- Weaver R., McCray R., Castor J., Shapiro P., Moore R., 1977, *ApJ*, 218, 377
- Woodward P. R., 1976, *ApJ*, 207, 484
- Xia X. Y., Xue S. J., Mao S., Boller T., Deng Z. G., Wu H., 2002, *ApJ*, 564, 196